

A full reconstruction of two galaxy clusters intra-cluster medium with strong gravitational lensing

Joseph F. V. ALLINGHAM^{1,2*}, Céline BÆHM¹, Dominique ECKERT³, Mathilde JAUZAC^{4,5,6,7},
David LAGATTUTA^{4,5}, Guillaume MAHLER^{4,5,8}, Matt HILTON^{6,7}, Geraint F. LEWIS¹,
and Stefano ETTORI^{8,9}

¹*School of Physics, A28, The University of Sydney, NSW 2006, Australia;*

²*Physics Department, Technion, 3200003 Haifa, Israel;*

³*Department of Astronomy, University of Geneva, ch. d'Écogia 16, CH-1290 Versoix Switzerland;*

⁴*Centre for Extragalactic Astronomy, Durham University, South Road, Durham DH1 3LE, UK;*

⁵*Institute for Computational Cosmology, Durham University, South Road, Durham DH1 3LE, UK;*

⁶*Wits Centre for Astrophysics, School of Physics, University of the Witwatersrand, Private Bag 3, 2050, Johannesburg, South Africa;*

⁷*Astrophysics Research Centre, School of Mathematics, Statistics & Computer Science, University of KwaZulu-Natal, Durban 4041, South Africa;*

⁸*STAR Institute, Quartier Agora - Allée du six Août, 19c B-4000 Liège, Belgium;*

⁹*INAF - Osservatorio di Astrofisica e Scienza dello Spazio di Bologna, via Piero Gobetti 93/3, 40129 Bologna, Italy;*

¹⁰*INFN, Sezione di Bologna, viale Berti Pichat 6/2, 40127 Bologna, Italy.*

Accepted 2024 January 08. Received 2023 December 22; in original form 2023 September 13

ABSTRACT

Whilst X-rays and Sunyaev-Zel'dovich observations allow to study the properties of the intra-cluster medium (ICM) of galaxy clusters, their gravitational potential may be constrained using strong gravitational lensing. Although being physically related, these two components are often described with different physical models. Here, we present a unified technique to derive the ICM properties from strong lensing for clusters in hydrostatic equilibrium. In order to derive this model, we present a new universal and self-similar polytropic temperature profile, which we fit using the X-COP sample of clusters. We subsequently derive an analytical model for the electron density, which we apply to strong lensing clusters MACS J0242.5-2132 and MACS J0949.8+1708. We confront the inferred ICM reconstructions to *XMM-Newton* and ACT observations. We contrast our *analytical* electron density reconstructions with the best canonical β -model. The ICM reconstructions obtained prove to be compatible with observations. However they appear to be very sensitive to various dark matter halo parameters constrained through strong lensing (such as the core radius), and to the halo scale radius (fixed in the lensing optimisations). With respect to the important baryonic effects, we make the sensitivity on the scale radius of the reconstruction an asset, and use the inferred potential to constrain the dark matter density profile using ICM observations. The technique here developed should allow to take a new, and more holistic path to constrain the content of galaxy clusters.

Key words: galaxies: clusters: intracluster medium, gravitational lensing: strong, X-rays: galaxies: clusters, galaxies: clusters: individual: MACS J0242.5-2132, galaxies: clusters: individual: MACS J0949.8+1708, hydrodynamics

1 INTRODUCTION

In the last decades, tremendous progress has been achieved in gravitational lensing observations (see Kneib & Natarajan 2011, for a review); from the first mass reconstruction of Abell 370 (Hammer 1987; Soucail et al. 1988) all the way to the *Hubble* Frontier Fields (HFF, Lotz et al. 2017), the Beyond the Ultra-deep Frontier Fields and Legacy Observations (BUFFALO, Steinhardt et al. 2020), and the numerous *JWST* lensing surveys (see e.g. UNCOVER, Bezanson et al. 2022). As a result, our understanding of this indirect observation of dark matter has improved, yet leaving open problems to discussions, such as the total matter (baryons & dark matter) potential distribution in galaxy clusters (Lilley et al. 2018; Roncadelli

& Galanti 2021), in particular in their outskirts (Trevisan et al. 2017), or the size of clusters themselves (see e.g. Chang et al. 2018; Tomooka et al. 2020; Baxter et al. 2021; Aung et al. 2023).

In parallel, the total matter distribution at large radii is assumed to be traced by the ionised intergalactic medium, the signature of which is detectable in the X-rays, and thanks to the Sunyaev-Zel'dovich (SZ) effect. While the projected lensing gravitational potential of galaxy clusters can be reconstructed from X-rays and SZ data through the Richardson-Lucy deprojection algorithm (see Konrad et al. 2013; Stock et al. 2015; Tchernin et al. 2018), the reverse path has not been explored yet. Efforts to relate the two observables range from Bulbul et al. (2010), describing the intra-cluster medium (ICM, composed of ionised gas) density through a dark matter (DM) profile and inferring the potential using the X-ray observation, to CLUMP-3D (see Sereno et al. 2013, 2017), exploiting the triaxial hypothesis to perform a

* E-mail: ajoseph@campus.technion.ac.il

joint ICM-lensing optimisation of the cluster physics, using disjoint models for the potential and the ICM thermodynamics.

We propose to predict the ICM thermodynamics using only the gravitational lensing-inferred potential. This should light our way towards a more holistic understanding of the dark matter profile, galaxy clusters thermodynamics, and interplay between baryons and dark matter. For instance, an offset between the lensing prediction and the X-ray observations could for instance hint towards interacting dark matter scenarios. In order to establish such a comparison, we convert the strong lensing detected gravitational potential into a predictive ICM model.

Deriving such a model requires to understand the thermodynamics of galaxy clusters. Making precise measurements from X-ray observations is limited by a series of assumptions, about e.g. the halo geometry (Buote & Humphrey 2012; Sereno et al. 2017), or the dynamical state of the cluster (Nelson et al. 2014; Biffi et al. 2016). Multiple studies have shown the hydrostatic regime to be an acceptable description of the ICM for cool-core and relaxing clusters (Ettori et al. 2013; Biffi et al. 2016; Vazza et al. 2018; Ettori et al. 2019). Conversely, recent mergers or dynamically disturbed systems present strong deviations to the hydrostatic equilibrium (Mahdavi et al. 2013). Moreover, galaxy clusters have followed a hierarchical model of formation, made of mergers and gravitational collapse. For this reason, their thermodynamics scales according to the cluster mass (Kaiser 1986; Bryan & Norman 1998), which is confirmed by simulations (Frenk et al. 1999; Borgani et al. 2005; Voit 2005) and observations (Ghirardini et al. 2019a). These assumptions (hydrostatic equilibrium, self-similarity) are common in joint X-rays and SZ analyses (cf. Capelo et al. 2012; Ghirardini et al. 2019a; Ghirardini et al. 2019b).

Using these assumptions, we adopted an effective polytropic temperature law in order to describe the thermodynamic model of the ICM of galaxy clusters (following e.g. Komatsu & Seljak 2001). Capelo et al. (2012) predicted a constant $\Gamma \sim 1.2$ polytropic index for the ICM in hydrostatic equilibrium with a NFW density profile, and Ghirardini et al. (2019b) recovered this value for the outskirts of clusters, but found radiative cooling to bring this value to $\Gamma \sim 0.8$ in the centre. In order to produce precise predictions *a priori*, we conduct a study of the polytropic index on the X-COP sample of data (described in Eckert et al. 2017). X-COP is a sample of 12 massive clusters selected from the *Planck* all-sky survey for which a deep X-ray follow-up with *XMM-Newton* was conducted (see Ghirardini et al. 2019a; CHEX-MATE Collaboration 2021). The thermodynamic properties of the ICM (pressure, temperature, density) were recovered over a broad radial range, which makes this sample ideal to derive the relation between the various thermodynamic quantities.

In Allingham et al. (2023), we analysed two galaxy clusters and reconstructed their gravitational potential with LENSTOOL (see Jullo et al. 2007) using strong gravitational lensing. Galaxy clusters MACS J0242.5-2132 and MACS J0949.8+1708, dynamically relaxed and relaxing respectively, provide the inputs to the ICM predictions for this work, and allow to justify the hydrostatic description of the ICM (Biffi et al. 2016). In this paper, we also test the β -model (see King 1966), commonly used by the X-ray and SZ communities to describe the ICM density distribution. We refer to it, and to the family of empirical models introduced in e.g. Vikhlinin et al. (2006) as *canonical*, in contrast to our models, which are derived analytically from the full matter density, using the Poisson and Euler equations, following the logic of Bulbul et al. (2010). As our *analytical* ICM models scale with the gravitational potential obtained with strong lensing, we directly work with the parameters of the lensing model.

After establishing the theoretical models, the quantitative ICM

results are confronted to the *XMM-Newton* and the ACT Data Release 5 millimetre-wave (see Naess et al. 2020; Mallaby-Kay et al. 2021). The quality of the reconstruction is tested with a MCMC on the density parameters, using these ICM data.

This article is structured as follows: the data are presented in Section 2; the strong lensing models are summarised in Section 3; the theoretical possible models for the electron density, the temperature, the gas fraction, the X-ray surface brightness and the SZ effect are introduced in Section 4; quantitative results for the density and temperature are presented in Section 5; the method to evaluate the quality of observational predictions follows up in Section 6; ICM predictions and MCMC optimisation results using the ICM observations are detailed in Section 7; a discussion on the limitations and possibilities of such a model is given in Section 8; and a summary and conclusion are provided in Section 9. We assume the Λ CDM cosmological model, with $\Omega_m = 0.3$, $\Omega_\Lambda = 0.7$, and $H_0 = 70 \text{ km.s}^{-1}.\text{Mpc}^{-1}$.

2 DATA

2.1 X-ray observations

2.1.1 MACS J0242 and MACS J0949

The ICM is primarily probed with X-ray observations. We used the *XMM-Newton* publicly available observations of the MACS J0242 and MACS J0949 in the 0.7-1.2 keV band (see CHEX-MATE Collaboration 2021). MACS J0242 was observed for a total of 70 ks (OBSID:0673830101), and MACS J0949 for a total of 36 ks (OBSID:0827340901). We analysed the two observations using XMM-SAS v17.0, and the most up-to-date calibration files. We used the XMM-SAS tools `mos-filter` and `pn-filter` to extract light curves of the observations and filter out periods of enhanced background, induced by soft proton flares. After flare filtering, the available clean exposure time is 61 ks (MOS) and 53 ks (PN) for MACS J0242, and 35 ks (MOS) and 34 ks (PN) for MACS J0949. The EPIC MOS filter maximises the signal-to-noise ratio, thus we used primarily these data. We extract the X-ray data following the procedure detailed through Ghirardini et al. (2019a), and the hydrostatic mass through Eckert et al. (2022).

With the NASA tool PIMMS, we get access to the conversion constants from flux to counts per second $C_{\text{flux}}^{\text{count}}$ for both clusters: for MACS J0242 and MACS J0949, $C_{\text{flux}}^{\text{count}} = 2.087 \times 10^{11}$ and $2.084 \times 10^{11} \text{ counts.erg}^{-1}.\text{cm}^2$ respectively¹.

2.1.2 The X-COP clusters

In order to tune our temperature and gas fraction models, we study a number of comparable clusters. The *XMM* cluster outskirts project (X-COP², described in Eckert et al. 2017) is ideal for this purpose: it gathers data from 12 massive clusters. These clusters are comparable to MACS J0242 and MACS J0949, with $3 \times 10^{14} M_\odot < M_{500} < 1.2 \times 10^{15} M_\odot$, but are in the redshift range $0.04 < z < 0.1$, smaller than for MACS J0242 and MACS J0949, at redshifts 0.313 and 0.383 respectively.

¹ The temperature of the ICM of both clusters being $> 3 \text{ keV}$, we can neglect the influence of temperature on the conversion constant.

² <https://dominiqueeckert.wixsite.com/xcop>

2.2 SZ observations

It is possible to study the ‘imprint’ of the ICM on the CMB through the SZ effect, which is seen as a deficit of CMB photons in the direction of clusters when observed at frequencies less than 217 GHz. With the Atacama Cosmology Telescope (ACT), we use the f090 and f150 ‘daynight’ DR5 maps³, centred on respective frequencies 97.8 and 149.6 GHz (see Hilton et al. 2021; Mallaby-Kay et al. 2021).

The BCG of MACS J0242 is a bright radio source, whose spectral energy distribution (SED) is detailed by Hogan et al. (2015). At 1 GHz, the source peaks at 1 Jy, making the extraction of the ICM signal with the SZ effect impossible. We thus only exploit the MACS J0949 data in this article.

3 STRONG LENSING ANALYSES OF MACS J0242 & MACS J0949

If distant background sources happen to be close to the line-of-sight between a massive galaxy cluster and an observer, the background image can be strongly lensed, to the point multiple images appear to the observer. Using this gravitational lensing effect in the strong regime, we can precisely map the gravitational potential of the cluster, and its total – baryonic and dark matter – mass density.

In Allingham et al. (2023), we performed a reconstruction of the total matter density, ρ_m , of the two galaxy clusters MACS J0242 and MACS J0949. These lensing models were obtained thanks to a combination of imaging with the *Hubble Space Telescope* (HST) and DES from the ground, together with spectroscopy obtained with the MUSE instrument at the Very Large Telescope (VLT). Figure 1 shows colour-composite images of the two clusters used in this work, together with the ICM distribution obtained using X-ray observations, and density contours from the strong-lensing analyses presented in Allingham et al. (2023).

With spectroscopy, we detected 6 and 2 systems of multiply-lensed images in MACS J0242 and MACS J0949 respectively, for a total of 18 and 9 images with spectroscopic redshifts. 4 additional systems were detected with imaging HST observations in cluster MACS J0949, but do not have a redshift measurement. Using a combination of photometry and spectroscopy, we identified 57 and 170 cluster member galaxies respectively. We performed the strong lensing optimisation with LENSTOOL (Jullo et al. 2007), using the multiply-imaged systems to invert the lens equation. We have assumed the potential of a galaxy cluster to be a superposition of dPIE potentials. We modelled each cluster with a large-scale dark matter halo (DMH), a brightest cluster galaxy (BCG), and a L^* catalogue of elliptical galaxies, scaled using the Faber-Jackson relationship (Faber & Jackson 1976). Additionally, we introduced in MACS J0949 a clump in the south of the halo, to explain multiply-lensed images in this region.

Tables 1 and 2 present respectively the summary of the lensing information available for each cluster, and the best-fit parameters of the strong-lensing models obtained for the different potentials of each galaxy clusters. The average distance between the multiple images predicted with the lensing models and the observations is 0.39'' and 0.15'', and the reduced χ^2 , $\chi_{\text{red}}^2 = 0.86$ and 0.67, for clusters MACS J0242 and MACS J0949 respectively, indicating a good quality reconstruction. The enclosed mass within 200 kpc of the cluster centre were respectively $M(R < 200 \text{ kpc}) = 1.67^{+0.03}_{-0.05} \times 10^{14} M_{\odot}$

for MACS J0242, and $M(R < 200 \text{ kpc}) = 2.00^{+0.05}_{-0.20} \times 10^{14} M_{\odot}$ for MACS J0949. Cluster MACS J0242 is found to be dynamically relaxed, with a peaked central density, while MACS J0949 presents a flatter density distribution in the core ($R \in [10, 100] \text{ kpc}$), and is still relaxing, but not strongly disturbed.

The inferred 3D density profiles were well fit by NFW profiles (see Section 4.1). For MACS J0242, we found the best fitting NFW parameters to be $\rho_S = 3.42 \times 10^{-25} \text{ g.cm}^{-3}$ and $r_S = 209.9 \text{ kpc}$, for a reduced $\chi^2 = 1.11$. For MACS J0949, the best fitting parameters are $\rho_S = 1.23 \times 10^{-25} \text{ g.cm}^{-3}$, $r_S = 405.5 \text{ kpc}$, for a reduced $\chi^2 = 1.90$. In this article, we only use the DMH and BCG potentials to represent the clusters’ gravitational potential.

4 GALAXY CLUSTERS: A THEORETICAL DESCRIPTION

This Section introduces the observables and models necessary to describe the physics of the ICM using gravitational lensing. Section 4.1 introduces the two general full matter density profiles we use in this work; Section 4.2 presents the *canonical* description for the ICM density; Section 4.3 shows the derivation of the *analytical* ICM density using a temperature model and total matter density; Section 4.4 extends the common polytropic temperature density to the higher electron densities found in the centre of clusters; Sections 4.5 and 4.6 define the X-ray surface brightness and the SZ effect temperature contrast respectively, in order to make observable predictions.

4.1 Galaxy clusters matter density models

The total matter density is modelled parametrically. We here present two cases, a Navarro-Frenk-White (NFW) density profile, and a dual Pseudo-Isothermal Elliptical mass distribution (dPIE) density profile. The generalised NFW and Einasto profiles are described in Appendix B. For the discussion and illustration purposes, we discuss purely radial profiles, but in our reconstruction, we use the various geometrical parameters of the individual potentials inferred from lensing (position of the centre, ellipticity, position angle).

4.1.1 Navarro–Frenk–White (NFW) profile

The NFW profile (introduced in Navarro et al. 1996) describes the DM density. We here approximate it to the total density distribution, ρ_m :

$$\rho_m(r) = \rho_S \left\{ \frac{r}{r_S} \left(1 + \frac{r}{r_S} \right)^2 \right\}^{-1}, \quad (1)$$

where ρ_S is the density normalisation, and r_S , the scale radius. These are parameters different for each cluster. We assume the NFW profile to describe the total density with one profile for a single cluster.

4.1.2 Dual Pseudo-Isothermal Elliptical mass distribution (dPIE) profile

In Kassiola & Kovner (1993) and Elíasdóttir et al. (2007), the dPIE profile scales as:

$$\rho_m(r) = \rho_0 \left\{ \left[1 + \left(\frac{r}{s} \right)^2 \right] \left[1 + \left(\frac{r}{a} \right)^2 \right] \right\}^{-1}, \quad (2)$$

with the core radius, a , of the order of 100 kpc for the dark matter halo, and a truncation radius, $s > a$. Whilst this distribution is spherically symmetric, we also consider two other parameters: a rotation angle,

³ https://lambda.gsfc.nasa.gov/product/act/actpol_dr5_coadd_maps_get.html

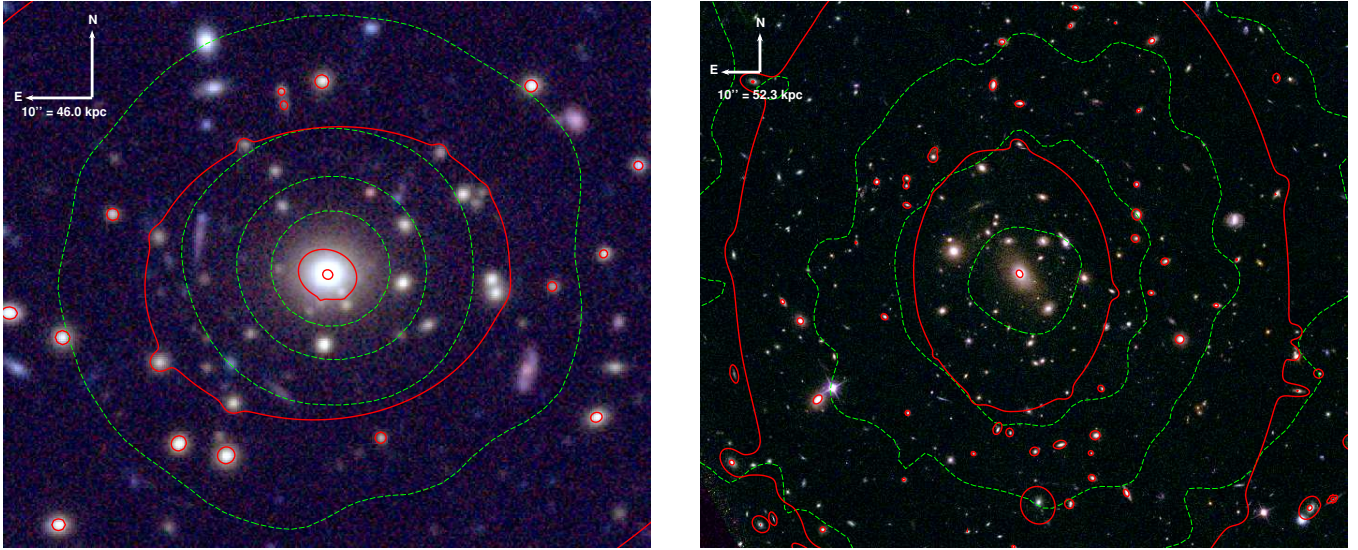


Figure 1. Composite RGB colour images of the two lensing clusters. *Left:* Composite DES colour image of MACS J0242. *Right:* Composite colour *HST* image of MACS J0949. *Green:* Hot gas distribution, obtained with *XMM-Newton* observations. *Red:* Contours of equal density, inferred from lensing models.

Table 1. Summary of the lensing reconstruction of galaxy clusters MACS J0242 and MACS J0949. We here list: (i) the galaxy clusters; (ii) number of galaxies in the cluster catalogue; (iii) number of multiply-lensed images detected; (iv) number of associated spectroscopic redshift measurements; (v) *rms* deviation of predicted multiply-lensed images positions from their observed positions in the image plane; (vi) reduced χ^2 ; (vii) projected mass enclosed within 200 kpc (in $10^{14} M_{\odot}$).

Galaxy cluster	N_{gal}	N_{im}	$N_{\text{spec-z}}$	<i>rms</i>	χ^2_{red}	$M(R < 200 \text{ kpc}) [10^{14} M_{\odot}]$
MACS J0242	57	18	18	0.39''	0.86	$1.67^{+0.03}_{-0.05}$
MACS J0949	170	20	9	0.15''	0.67	$2.00^{+0.05}_{-0.20}$

Table 2. Best fit parameters of the strong lensing mass model for MACS J0242 and MACS J0949. We here list the central coordinates, Δ_{α} and Δ_{δ} , in arcsec, relative to the centre, the ellipticity, e , the position angle in degrees, θ , the core radius in kpc, a , the cut radius in kpc, s , and the velocity dispersion in km.s^{-1} , σ , for each component of the model. The centres are taken to be respectively $(\alpha_c, \delta_c) = (40.649555, -21.540485)$ deg and $(\alpha_c, \delta_c) = (147.4659012, 17.1195939)$ deg for MACS J0242 and MACS J0949. The asterisks highlight parameters which are fixed during the optimisation. L^* represents the cluster member galaxies catalogue, scaled with the Faber-Jackson scaling relation (Faber & Jackson 1976). MACS J0949 includes a southern dark matter clump O3.

	Δ_{α} [arcsec]	Δ_{δ} [arcsec]	e	θ [deg]	a [kpc]	s [kpc]	σ [km.s^{-1}]
MACS J0242							
DMH	$-0.14^{+0.09}_{-0.14}$	$0.14^{+0.11}_{-0.18}$	$0.29^{+0.04}_{-0.03}$	$17.9^{+0.8}_{-1.8}$	$57.2^{+6.0}_{-8.4}$	1500*	$918.5^{+29.0}_{-36.1}$
BCG	0.04^*	-0.09^*	0.23^*	$155.8^{+10.8}_{-9.6}$	0.30^*	$177.6^{+32.2}_{-58.0}$	$524.5^{+58.8}_{-44.0}$
L^*					0.03^*	$5.6^{+7.8}_{-1.8}$	$199.2^{+30.7}_{-53.3}$
MACS J0949							
DMH	$-1.94^{+0.22}_{-2.84}$	$-0.67^{+0.57}_{-0.67}$	$0.25^{+0.40}_{-0.05}$	$92.4^{+0.6}_{-1.3}$	$116.2^{+24.1}_{-51.7}$	1500*	$1236.1^{+59.3}_{-310.6}$
BCG	0^*	0^*	0.48^*	120.1^*	0.25^*	$98.0^{+153.7}_{-34.3}$	$253.7^{+196.5}_{-18.5}$
Clump O3	$4.80^{+0.75}_{-0.46}$	$-60.13^{+2.39}_{-1.42}$	$0.01^{+0.29}_{-0.06}$	$128.6^{+41.4}_{-27.5}$	$20.5^{+31.6}_{-8.8}$	$232.5^{+180.1}_{-119.9}$	$323.2^{+120.2}_{-54.9}$
L^*					0.15^*	$23.1^{+111.5}_{-2.1}$	$139.3^{+25.8}_{-18.5}$

θ , and an ellipticity, e (see Appendix A). This model is sometimes referred to as *pseudo-Jaffe*, as in the review of Keeton (2001).

Contrarily to the NFW density profile, the dPIE profile does not present any divergence in $r \rightarrow 0$, i.e. presents a finite density in the core. For our lensing reconstruction, we used a large scale DMH modelled with a dPIE, and superposed it to individual profiles fit-

ting individual cluster member galaxies. In the case of the analysed clusters, their (relative) relaxation allows us to discard all individual (galaxy) potentials but that of the BCG. The DMH and the BCG respectively govern the large and small radii total matter densities. This DMH and BCG superposition was well fitted by a NFW profile for both clusters (see Section 3).

4.2 Electron density

We focus on the electron density n_e because it can be derived from X-ray observations. However, one could derive the ion or gas density too. The number density of electrons, n_e , is related to the gas volume density, ρ_g through:

$$n_e(r) = \mathcal{F}_I(r) \frac{\rho_g(r)}{\mu_e m_a}, \quad (3)$$

where \mathcal{F}_I is the local ionisation fraction which is taken to be 1, $m_a = 1 \text{ Da}$ is the atomic mass constant, and $\mu_e \approx 1.15$ is the mean molecular weight of electron.

A number of models have been proposed to fit the electron density profile, which we refer to as *canonical*. One of the most complete model can be found in Vikhlinin et al. (2006). As this model relies on a large set of parameters, unnecessary here, we shall focus on a simplified model, namely the (simple) β -model (see King 1966; Cavaliere & Fusco-Femiano 1976):

$$n_e(r) = n_{e,0} \left[1 + \left(\frac{r}{r_c} \right)^2 \right]^{-\frac{3}{2}\beta}, \quad (4)$$

with r_c , the core radius, $n_{e,0}$ a density normalisation, and $\beta \in [0.5; 0.9]$, an empirical index. We find this model to fit well both clusters' ICM distribution (see Sections 7.1.1 and 7.2.1), thus showing a more complex model to be unnecessary here.

4.3 A fully analytical electron density

4.3.1 General case

We consider the total (DM and baryons) mass density as a sum of densities:

$$\rho_m(r) = \sum_i \rho_{0,m,i} f_i(r), \quad (5)$$

which is constrained by the strong lensing analyses. Each potential can be normalised differently, and the distributions, f_i , are assumed to be of the same type (here NFW or dPIE). Here, we write them as a sum of radial functions for simplicity. In practice, every profile, f_i , has its own geometric parameters (central position, ellipticity, rotation angle), which we consider to be fixed from the strong lensing analysis.

Assuming integrability, we introduce:

$$\begin{aligned} g_i(r) &= \int_0^r ds s^2 f_i(s), \\ h_i(r) &= \int_0^r ds s^{-2} g_i(s), \end{aligned} \quad (6)$$

where integration constants are included. Denoting Φ the Newtonian potential, integrating the gravitational Poisson equation, it reads:

$$\Phi(r) = -4\pi G \sum_i \rho_{0,m,i} h_i(r). \quad (7)$$

The conservation of momentum in the Lagrangian formalism, i.e. the momentum Navier-Stokes equation for a perfect fluid (viscosity neglected, see e.g. Landau & Lifshitz 1959) reads:

$$\rho_g \frac{D\mathbf{v}}{Dt} = \rho_g [\partial_t \mathbf{v} + (\mathbf{v} \cdot \nabla) \mathbf{v}] = -\nabla P_g + \rho_g \nabla \Phi, \quad (8)$$

with \mathbf{v} the velocity field, and P_g the gas pressure.

As the pressure in galaxy clusters is of the order of 10^{10} Pa , the plasma is thermalised, and therefore the temperature of the ions is

equal to that of the electrons. With equation (3), we can write the number density of the electron n_e as being directly proportional to the gas density ρ_g , as μ_e and \mathcal{F}_I are assumed to be constant in a given cluster. Using the ideal gas law, we rewrite equation (8) in the purely radial case:

$$\frac{k_B}{\mu_g m_a} \frac{\partial_r (n_e T_e)}{n_e} + \partial_t v_r + v_r \partial_r v_r = -4\pi G \sum_i \rho_{0,m,i} r^{-2} g_i(r), \quad (9)$$

where T_e is the electron temperature, $\mu_g \approx 0.60$ mean molecular weight of the gas, and k_B the Boltzmann constant. As the galaxy clusters used in our study are not strongly perturbed, we work under the hypothesis of hydrostatic equilibrium. Assuming we could decompose the velocity in its radial and temporal dependencies, one could then integrate numerically. As we do not have access to the ICM velocity resolution, we here assume a polytropic temperature distribution and the stream to be hydrostatic, i.e. of constant velocity both in time and in all spatial directions (see e.g. Zaroubi et al. 2001). Thus, with $\partial_t v_r = \partial_r v_r = 0$, we get:

$$\frac{\partial_r (n_e T_e)}{n_e} = \epsilon \sum_i \rho_{0,m,i} r^{-2} g_i(r), \quad (10)$$

where $\epsilon = -4\pi G \mu_g m_a / k_B$.

In order to reduce this expression, we define a general \mathcal{J} function which contains information on the temperature profile as:

$$\mathcal{J}(n_e) = \int_0^{n_e} \frac{d[nT_e(n)]}{T_0 n}, \quad (11)$$

where T_0 is a temperature normalisation (see Sect. 4.4). More details on the definition of \mathcal{J} are given in Sect. 5.1, given a precise temperature model.

Separating variables and integrating equation (10), we obtain:

$$\mathcal{J}(n_e) = \frac{\epsilon}{T_0} \sum_i \rho_{0,m,i} h_i(r) = \frac{\mu_g m_a}{k_B T_0} \Phi(r), \quad (12)$$

where the right-handed term stems from equation (7). If we assume \mathcal{J} to be bijective⁴ (which is justified given a temperature model in Sect. 5.1), then inverting this equation simply provides $n_e(r)$:

$$n_e(r) = \mathcal{J}^{-1} \left(\frac{\mu_g m_a}{k_B T_0} \Phi(r) \right). \quad (13)$$

Under reasonable physical hypotheses, we have provided a general, completely *analytical* description of the electron density using only the gravitational potentials characterised with strong lensing observations. To allow this reconstruction to be independent from other observations, we need to pair this analytical model with an electron temperature model.

4.3.2 Case of a dPIE density

In the case of a dPIE profile, we give:

$$\begin{aligned} f(r) &= \left\{ \left[1 + \left(\frac{r}{s} \right)^2 \right] \left[1 + \left(\frac{r}{a} \right)^2 \right] \right\}^{-1}, \\ g(r) &= \frac{a^2 s^2}{a^2 - s^2} \left[a \arctan \frac{r}{a} - s \arctan \frac{r}{s} \right], \\ h(r) &= \frac{a^2 s^2}{a^2 - s^2} \left[\frac{s}{r} \arctan \frac{r}{s} - \frac{a}{r} \arctan \frac{r}{a} + \frac{1}{2} \ln \left(\frac{r^2 + s^2}{r^2 + a^2} \right) \right], \end{aligned} \quad (14)$$

⁴ A bijective function $f : \mathcal{X} \rightarrow \mathcal{Y}$ associates to each element of a set \mathcal{X} an image of set \mathcal{Y} , and reciprocally. Therefore, a function is invertible if and only if it is bijective.

where a and s represent the core r_{core} and scale r_{cut} radii of the i -th dPIE potential respectively. Indices were avoided for clarity. To avoid confusion, we write idPIE the n_e distribution with h_i given by a dPIE.

4.3.3 Case of a NFW density

In the case of a NFW potential (see equation 1), we can rewrite the different integrals given equation (14) for the dPIE:

$$\begin{aligned} f(r) &= \left\{ \left[\frac{r}{r_S} \right] \left[1 + \frac{r}{r_S} \right]^2 \right\}^{-1}, \\ g(r) &= r_S^3 \left[\ln \left(1 + \frac{r}{r_S} \right) - \frac{r}{r+r_S} \right], \\ h(r) &= -\frac{r_S^3}{r} \ln \left(1 + \frac{r}{r_S} \right). \end{aligned} \quad (15)$$

Here $\rho_{0,m,i}$ of equation (12) is $\rho_{S,m}$. In case of a NFW profile, we assume the total density to be represented by a single profile. We shall write the resulting n_e distribution idNFW .

4.4 Temperature

In order to derive the ICM density and thermodynamic profiles using strong lensing constraints only, we need to adopt a general temperature model, independent of the specific observations of one cluster. We shall consider polytropic models (for example in [Capelo et al. 2012](#)) of the form :

$$T_e(r) = T_0 \left(\frac{n_e(r)}{n_0} \right)^{\Gamma-1}, \quad (16)$$

with n_0 the central electronic density, T_0 the temperature in the centre, and $\Gamma \approx 1.2$, the polytropic index.

Following [Ghirardini et al. \(2019b\)](#), we can extend this definition to a self-similar polytropic temperature model, with a varying polytropic index, $\Gamma(n_e)$:

$$\begin{aligned} \frac{P_e}{P_{500,c}} &= \eta_P \left(\frac{n_e E(z)^{-2}}{\eta_n} \right)^{\Gamma(n_e)}, \\ \frac{T_e}{T_{500,c}} &= \eta_T \left(\frac{n_e E(z)^{-2}}{\eta_n} \right)^{\Gamma(n_e)-1}, \end{aligned} \quad (17)$$

where $E(z) = H(z)/H_0$ is the normalised Hubble factor assuming a Λ CDM cosmology with $\Omega_m = 0.3$ and $\Omega_\Lambda = 0.7$. η_P and η_T are dimensionless proportionality constants, and η_n the volume number density normalisation. We write $T_0(z) = \eta_T T_{500}(z)$ and $n_0(z) = \eta_n E(z)^2$. Section 5.1.2 presents a new model for the index $\Gamma(n_e)$, and also provides the quantitative values for the different constants presented here.

4.5 X-ray surface brightness

In order to compare our results to observations, and therefore to evaluate the quality of our ICM reconstruction, we introduce the X-ray surface brightness S_X (see [Böhringer & Werner 2010](#), for a review). In a band of wavelength (such as the [0.7, 1.2] keV band for *XMM-Newton*) integrated over the line-of-sight, it reads:

$$S_X(\Delta E) = \frac{1}{4\pi(1+z)^4} \frac{\mu_e}{\mu_H} \int_0^\infty n_e^2(r) \Lambda(\Delta E, T_e, Z) dl. \quad (18)$$

where $\mu_H \approx 1.35$ is the mean molecular weight of hydrogen, $\Lambda(\Delta E, T_e, Z)$ is the X-ray spectral emissivity (or *cooling curve*), as a function of the X-ray energy band, ΔE , the electron temperature of the gas, T_e , and the metallicity of the gas, Z . In this article, the metallicity is assumed to be constant for a given cluster.

4.6 SZ effect

Another observable, depending on the electron density and temperature is the SZ effect. Given an observable frequency, ν , we use the reduced frequency, x :

$$x = \frac{h\nu}{k_B T_r}, \quad (19)$$

with h , the Planck constant, and $T_r \approx 2.726$ K, the temperature of the CMB. We define the Compton parameter (see [Rephaeli 1995](#)):

$$y(r) = \frac{k_B \sigma_T}{m_e c^2} \int_0^\infty T_e(r) n_e(r) dl, \quad (20)$$

with σ_T , the Thomson cross-section, and m_e , the mass of the electron. The thermal SZ contrast then reads:

$$\Theta_{\text{SZ}}(r) = \frac{\Delta T}{T_r} = \left[x \coth \left(\frac{x}{2} \right) - 4 \right] y(r). \quad (21)$$

5 QUANTITATIVE MODELS

We have presented in the previous section a completely different manner to use the lensing study of galaxy clusters to predict their baryonic distributions. Assuming the hydrostatic equilibrium and a given temperature distribution, equation (13) presents an *analytical* ICM density prediction using lensing. Moreover, in Appendix D1, we present an alternative method, reducing the gas fraction to an analytical model, and using knowledge of ρ_m , constrained by lensing analysis. Although the general profile of the gas fraction is retrieved, this study is however not completely generalisable, and we do not use it here.

In this section, we provide the electron temperature models needed for the analytical method. We make quantitative estimates in order to yield quantitative predictions for ICM density profile from lensing data only.

5.1 Polytropic index scaling

5.1.1 Constant polytropic index

As shown in Sect. 4.3, one can reconstruct the ICM profile using equation (13) and an analytical expression for the function \mathcal{J} which contains the information about the electron temperature profile. Here, we assume the following form for \mathcal{J} , based on a self-similar polytropic temperature law with a constant index $\gamma > 1$ (see equation 17):

$$\mathcal{J}_z(n_e) = \frac{\gamma}{\gamma-1} \left(\frac{n_e}{n_0(z)} \right)^{\gamma-1}. \quad (22)$$

We can write the electron density from equation (12):

$$n_e = n_0(z) \left[\frac{\gamma-1}{\gamma} \frac{\epsilon}{T_0(z)} \sum_i \rho_{0,m,i} h_i(r) \right]^{1/(\gamma-1)}. \quad (23)$$

However, we find such a description to fail to describe the higher electron densities ($n_e > 10^{-2} \text{ cm}^{-3}$), which is consistent with a constant γ index fixed with the largest radii of clusters, i.e. the least

dense regions. We notice the specific case of a polytropic temperature density associated to a NFW profile has already been studied in [Bulbul et al. \(2010\)](#), where a self-normalisation in the centre is utilised.

5.1.2 Polytropic index model

To describe the relation between ICM thermodynamic quantities (n_e , P_e , T_e), it is common practice to describe the stratification of the ICM using a polytropic equation of state $P(n_e) \propto n_e^\Gamma$ (e.g. [Bulbul et al. 2010](#); [Capelo et al. 2012](#); [Tchernin et al. 2018](#); [Ghirardini et al. 2019b](#)). Analytic models assuming the ICM to be in hydrostatic equilibrium within a NFW potential predict that the polytropic index Γ should be close to a constant value of ~ 1.2 throughout the cluster volume ([Capelo et al. 2012](#)). Observationally speaking, the measured values of the polytropic index closely match the NFW expectation in cluster outskirts ($R > 0.2R_{500}$), but significantly deviate from it in the cluster core, where Γ decreases down to ~ 0.8 under the influence of radiative cooling ([Ghirardini et al. 2019b](#)). Using the data from the X-COP programme, [Ghirardini et al. \(2019b\)](#) showed that the $P(n_e)$ relation is nearly universal across the cluster population with a low scatter of $\sim 15\%$, independently of a system's dynamical state. Here we propose a new functional form to describe the self-similar polytropic model (supported by e.g. [Mostoghiu et al. 2019](#)). We describe the relation with a smoothly varying polytropic index $\Gamma(n_e)$ as:

$$\frac{d \ln P_e}{d \ln n_e} \equiv \Gamma(n_e) = \Gamma_0 \left[1 + \Gamma_S \arctan \left(\ln \frac{n_e E(z)^{-2}}{\eta_n} \right) \right], \quad (24)$$

with η_n the reference number density around which the transition between core (low Γ) and outskirts (NFW Γ) occurs, Γ_0 the polytropic index at η_n , and Γ_S the slope of the transition.

We used the publicly available X-COP data, which provide high-quality observations of the ICM thermodynamic properties over a wide radial range ($\approx [0.01 - 2]R_{500}$), to calibrate the model and determine the parameters of equation (24). We fit the X-COP density and pressure data using the Bayesian analysis package PyMC3 ([Salvatier et al. 2016](#)), including uncertainties on both axes, and a free log-normal intrinsic scatter. The observational data points on both axes are scaled by their respective self-similar scaling values ([Arnaud et al. 2010](#)). The result of this procedure is shown in Fig. 2. The model provides an excellent representation of the data over three decades in electron density, with a low intrinsic scatter of $\sigma_{\ln P} = 0.19 \pm 0.02$. The right-hand panel of Fig. 2 also shows that the results obtained with the model defined in equation (24) are consistent with the values estimated by [Ghirardini et al. \(2019b\)](#) when fitting a piece-wise power law over several ranges in density. The fit parameters are included in Table 3.

Supposing the ICM to be an ideal gas, following [Ghirardini et al. \(2019a\)](#), we write:

$$\eta_T = \left(3.87 \times 10^{-4} \text{ cm}^{-3} \right) \frac{\eta_P}{\eta_n} \frac{f_b}{0.16} \frac{\mu_e}{1.14}, \quad (25)$$

with f_b is the universal baryon fraction, taken to be $f_b = 0.158 \pm 0.002$ ([Ade et al. 2016](#)). We find $\eta_T \approx 1.034$.

As for the full $T_{500}(z)$, we use the results of [Ghirardini et al. \(2019a\)](#), which we reproduce here:

$$T_{500}(z) = 8.85 \text{ keV} \left(\frac{M_{500} E(z)}{h_{70}^{-1} 10^{15} M_\odot} \right)^{2/3} \left(\frac{\mu_g}{0.6} \right), \quad (26)$$

with $h_{70} = h/0.7 = 1$. We therefore can normalise the temperature universally.

5.1.3 Varying polytropic index

At a given redshift, z , using the self-similar polytropic temperature described equations (17) and (24), we can define the integral \mathcal{J}_z , i.e. a redshift dependent \mathcal{J} , defined equation (11):

$$\mathcal{J}_z(n_e) = \int_0^{n_e} \left[\Gamma(n) + \frac{\Gamma_0 \Gamma_S \ln \left(\frac{n}{n_0(z)} \right)}{1 + \left[\ln \left(\frac{n}{n_0(z)} \right) \right]^2} \right] \left(\frac{n}{n_0(z)} \right)^{\Gamma(n)-1} n^{-1} dn. \quad (27)$$

In this case, \mathcal{J}_z can be easily computed at a given redshift, and reverted. It is however not analytically solvable. An example of \mathcal{J}_z is displayed in Fig. 3.

We find empirically \mathcal{J}_z to be a monotonically increasing function, i.e. a bijection. Therefore we can take its inverse function, allowing to define n_e as a function of the radius, as displayed in equation (13).

5.2 Relating all density models to lensing

We assume the metallicity of clusters MACS J0242 and MACS J0949 to be constant, and the plasma to be fully ionised $\mathcal{F}_I = 1$. The X-ray data suggest metallicities in the range $0.2 - 0.7 Z_\odot$ for the two strong lensing clusters. The metallicity profiles obtained are in agreement with the $Z = 0.3 Z_\odot$ in both clusters, and we therefore make this assumption. Moreover, the influence of metallicity on the cooling function is limited at these temperatures (to justify this approximation, read e.g. [McDonald et al. 2016](#)).

For the analytical density profiles (such as idPIE or iNFW), the parameter priors are directly given from the lensing analysis Sect. 3. Conversely, we can not assume the parameters of the β -profile *a priori*. However their optimisation requires priors, for which we take $\beta = 0.63$ (in agreement with e.g. [Böhringer et al. 2016](#)), $n_{e,0}$ is taken to be the normalisation of the DMH density, and r_c to be a_1 , i.e. the core radius of the DMH obtained with the lensing optimisation.

6 METHOD: MEASURABLE ICM PREDICTIONS AND OPTIMISATIONS

In this Section, we present the results of the method developed in Sections 4 and 5 to convert the ICM predictions into ICM observables (S_X , Θ_r), in order to compare them to observations. Moreover, we contrast these predictions with a profile of the same type (e.g. idPIE) optimised with a MCMC using the ICM observations. We summarise the whole process undertaken in the present article in Fig. 4.

6.1 Point spread function of XMM-Newton

In order to analyse the XMM-Newton observations, we reduce them to smaller maps centred around the cluster, of around 1 Mpc width (respectively 88 and 78 pixels for clusters MACS J0242 and MACS J0949). We then need to take into account the point-spread function (PSF). At first order, we define the PSF as:

$$PSF(r) = \left[1 + \left(\frac{r}{r_0} \right)^2 \right]^{-\alpha}, \quad (28)$$

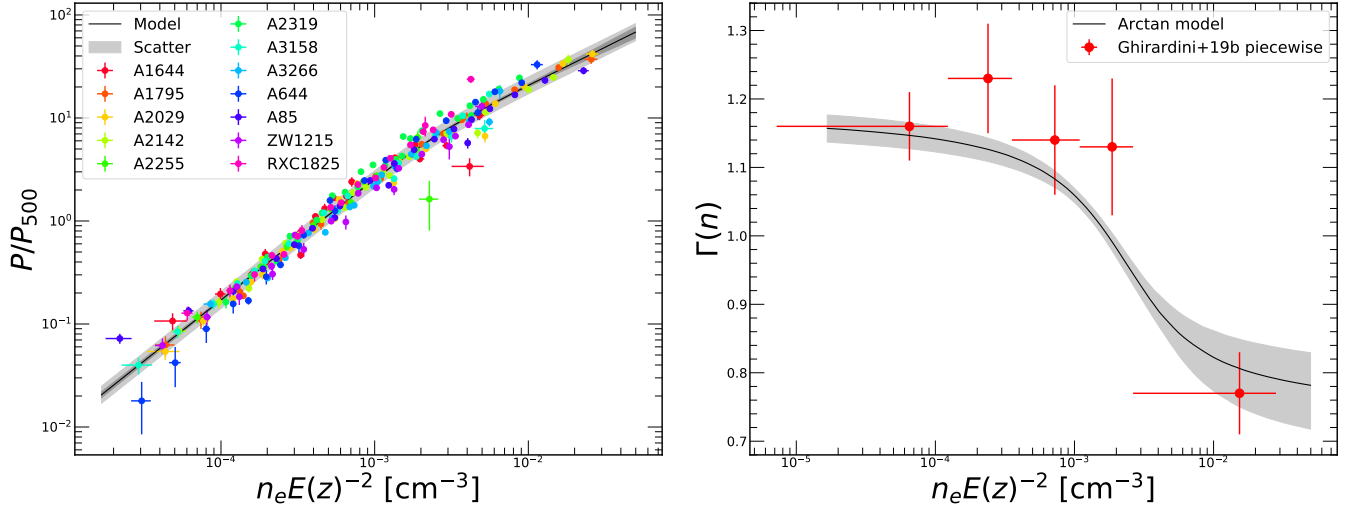


Figure 2. Calibration of the variable $\Gamma(n_e)$ polytropic model (equation 24) on X-COP data. *Left:* Relation between self-similar scaled ICM pressure and electron density for the 12 X-COP clusters. The solid black line and the grey shaded area show the best-fit model and the intrinsic scatter around the model, respectively. *Right:* Polytropic index $\Gamma = d \ln P_e / d \ln n_e$ as a function of electron density. The black line and shaded area shows the best-fit model with equation (24), whereas the red data points show the result of a piece-wise fit with constant polytropic index over several ranges in electron density.

Table 3. Parameters of the smoothly varying polytropic model defined in equations (17) and (24).

η_P	η_n [cm $^{-3}$]	Γ_0	Γ_S	$\sigma_{\ln P_e}$
6.05 ± 1.57	$(2.26 \pm 0.59) \times 10^{-3}$	0.97 ± 0.04	-0.15 ± 0.03	0.19 ± 0.02

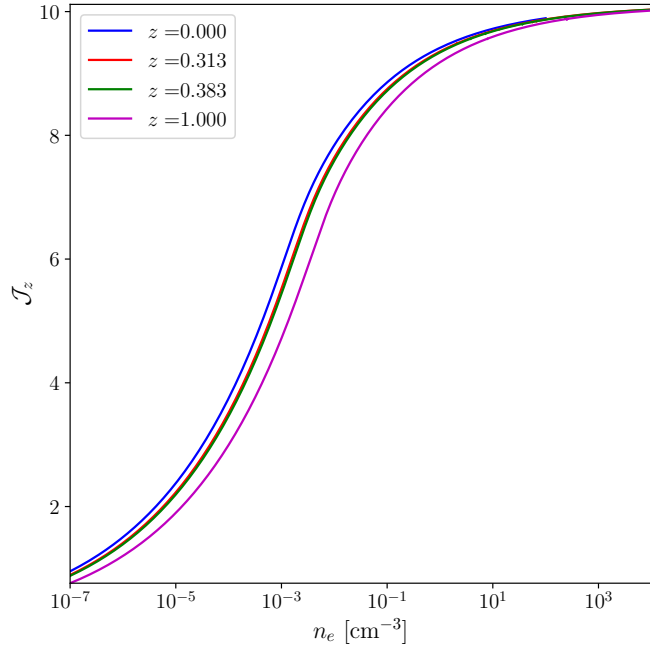


Figure 3. $\mathcal{J}_z(n_e)$ in a range of redshifts, including those of galaxy cluster MACS J0242 and MACS J0949 – which are almost identical. The \mathcal{J}_z function is therefore extremely sensitive, i.e. a small error on the potential is associated to a much larger error in the determination of n_e .

with r the distance to the centre, $r_0 = 5.304$ arcsec and $\alpha = 1.589^5$. We note that the number of pixels of the PSF must be odd to account for the centre. The measured surface brightness writes:

$$S_X^{\text{conv}}(x, y) = (S_X^{\text{model}} \otimes \text{PSF})(x, y) \quad (29)$$

where S_X^{model} is provided in equation (18).

As the edge effect is quite important, we decide not to use the borders, and to cut 8 pixels on each side of the map. The final comparison maps are respectively 72 and 62 pixels wide for MACS J0242 and MACS J0949. We note that we still have to compute our model for the full width of the original maps, as they are needed in the convolution.

6.2 Converting surface brightness into count signal

We use the EPIC count maps of *XMM-Newton*, masking point-like sources, including diffuse emission only. As we also have access to the time of exposure, E , and total background, B (particle background, soft protons, PN chip out-of-time events), maps from surface brightness models, we can make predictions on the number count of detection:

$$N_{X,c} = C_{\text{flux}}^{\text{count}} S_X^{\text{conv}} \times E + B + C_{\text{sky}} \quad (30)$$

where C_{sky} is the sky constant, measured in the empty regions of the raw count map.

⁵ https://xmm-tools.cosmos.esa.int/external/xmm_calibration/calib/documentation/epic_cal_meetings/200111/PSF-MOS_Ghizzardi.pdf

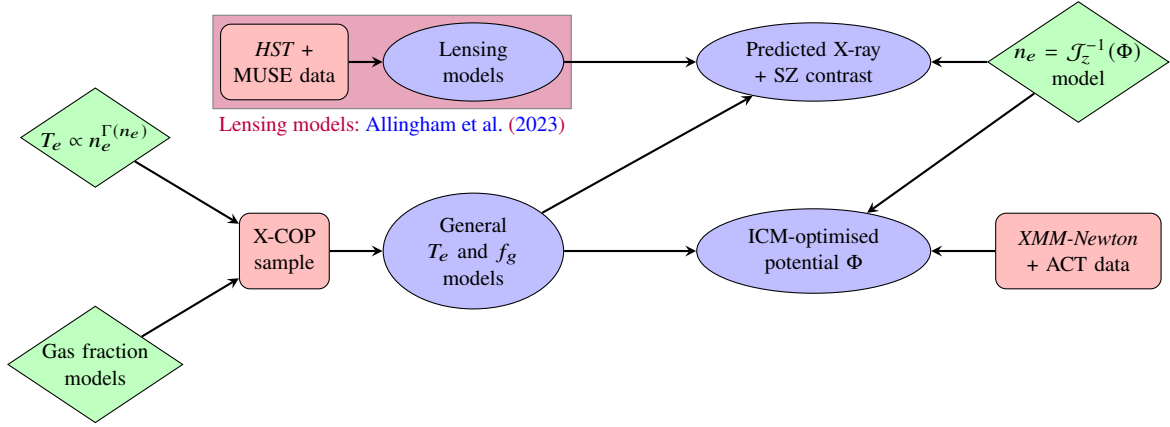


Figure 4. Full workflow diagram. Models are denoted by green diamonds, data by red rectangles, while results are in blue ellipses. The light magenta rectangle denotes work carried out within our previous companion article Allingham et al. (2023).

We also take dust absorption into account, with the absorption ratio (see e.g. Wilms et al. 2000):

$$\frac{I_{\text{obs}}}{I_{\text{em}}} = \exp \left[-n_H^{\text{gal}} \sigma(E_X) \right], \quad (31)$$

where n_H^{gal} is the galactic hydrogen, and σ , the extinction cross-section of that same dust for a photon energy, E_X . We report absorption factors of 0.9439 and 0.9398 for clusters MACSJ0242 and MACSJ0949 respectively.

6.3 Cooling curve

In order to access the X-ray spectral emissivity, $\Lambda(\Delta E, T_e, Z)$, mentioned in equation (18), we use *AtomDB* (see Foster et al. 2012). With the metallicities of set Asplund et al. (2009) adjusted to our $Z_{\text{cl}} = 0.3Z_{\odot}$, we can plot the cooling curve in the energy band of *XMM-Newton* (adjusted for K-correction). The results at the redshifts of clusters MACSJ0242 and MACSJ0949 are displayed in Fig. 5.

6.4 Sunyaev-Zel’dovich maps filtering

We simply filter both ACT DR5 map $\Theta_{r,f}^{\text{obs}}$ of MACSJ0949 with a Gaussian filter of radius 0.05 degrees $\mathcal{G}(0.05 \text{ deg})$, with *NEMO*⁶. We then subtract it from the original map, thus high-pass Gaussian filtering the original map. Although this does not allow to fully remove either the CMB signal or the atmosphere variability, at the scale of the cluster, it allows to smooth and attenuate the CMB variability. In order to compare our SZ effect model to the filtered data maps, we convolve the modelled signal map $\Theta_{r,f}^{\text{mod}}$ with the ACT beam \mathcal{B}_f at the map frequency f . This allows to take the telescope PSF into account. We further apply the Gaussian filter, and compare the resulting maps:

$$\begin{aligned} \Theta_{r,f}^{\text{obs, filt}} &= \Theta_{r,f}^{\text{obs}} - \Theta_{r,f}^{\text{obs}} \otimes \mathcal{G}(0.05 \text{ deg}), \\ \Theta_{r,f}^{\text{mod, filt}} &= \left(\Theta_{r,f}^{\text{mod}} \otimes \mathcal{B}_f \right) \otimes \mathcal{G}(0.05 \text{ deg}). \end{aligned} \quad (32)$$

In a similar fashion to that of the X-ray PSF, we have to remove the borders of the SZ filtered image because of border effects. We

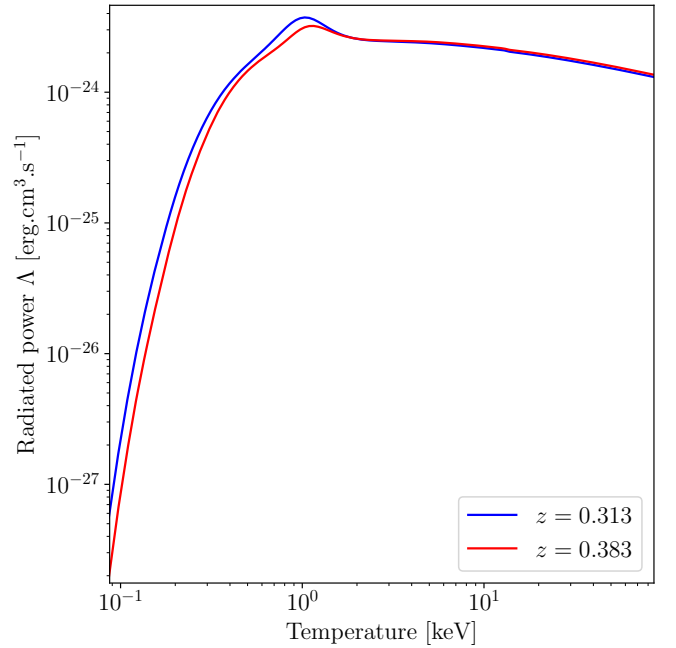


Figure 5. Radiated power (cooling curve) for a metallicity $Z = 0.3Z_{\odot}$, using the metallicities described in Asplund et al. (2009), in the band [0.7; 1.2] keV, at the respective redshift of MACSJ0242 (blue) and MACSJ0949 (red).

therefore used model maps of ~ 4 Mpc initially (26 pixels), reduced to ~ 2 Mpc (14 pixels), and compared these predictions to the ACT DR5 filtered data.

6.5 Working hypotheses on the density distribution

We based our analysis on the mass models described in our previous work (Allingham et al. 2023). We model the total mass profile of MACSJ0242 and MACSJ0949 using strong lensing constraints of radii ranging in $R \in [50, 200]$ kpc. While we acknowledge the limitations of the constraining power, we extrapolate the 3D density out to $R_{500,c}$, and recover a mass $M_{500,c} = 5.95^{+0.40}_{-0.46} \times 10^{14} M_{\odot}$ and

⁶ <https://nemo-sz.readthedocs.io>

Table 4. Best fit of all optimisation models for cluster MACS J0242. The columns are as follows: (i) The observation type used to constrain the profile. (ii) The profile type. (iii) $\rho_{0,1}$ denotes the DMH central density in the case of idPIE profile, ρ_S in the iNFW case, and the central gas density ρ_c in the case of a β -profile. All density values are displayed in g.cm^{-3} . (iv) a_1 denotes the DMH core radius in the idPIE model, r_S the scale radius in the iNFW case, and r_c in the β -model. All of these distances are displayed in kpc. (v) s_1 denote respectively the cut radius of the DMH and of the BCG, in the case idPIE. (vi) $\rho_{0,2}$ denotes the BCG central density in the idPIE case. (vii) s_2 is the cut radius of the BCG. (viii) β is the power index of the β profile. (ix) $-\ln \mathcal{L}_X$ is the negative log-likelihood evaluated on X-rays data. When a parameter set is out of the invertible range of function \mathcal{F}_z (i.e. $\sim [0, 10]$), we denote the log-likelihood $\ln \mathcal{L}$ as infinite. For cluster MACS J0242, the optimisation is only performed with *XMM-Newton* data. The core radius of the BCG a_2 is fixed for both the lensing and ICM optimisations. Starred values were fixed. We find the optimisation of s_2 to be degenerate; we therefore fix this parameter.

Observation	Profile	$\rho_{0,1}, \rho_S$ or ρ_c	a_1, r_S or r_c	s_1	$\rho_{0,2}$	s_2	β	$-\ln \mathcal{L}_X$
Unit		$[\text{g.cm}^{-3}]$	$[\text{kpc}]$	$[\text{kpc}]$	$[\text{g.cm}^{-3}]$	$[\text{kpc}]$		
Lensing	dPIE	$1.0^{+3.4}_{-0.2} \times 10^{-24}$	$57.2^{+6.0}_{-8.4}$	1500*	$1.2^{+0.3}_{-0.2} \times 10^{-20}$	$177.6^{+32.2}_{-58.0}$	–	∞
	NFW	$3.4^{+0.5}_{-0.4} \times 10^{-25}$	$209.9^{+17.1}_{-15.8}$	–	–	–	–	∞
ICM (X-rays only)	β	$2.6^{+11.0}_{-1.8} \times 10^{-23}$	$17.9^{+38.1}_{-13.3}$	–	–	–	$0.54^{+0.20}_{-0.08}$	0.68
	idPIE	$5.3^{+9.3}_{-2.4} \times 10^{-25}$	$73.0^{+34.7}_{-23.2}$	2720^{+460}_{-890}	$4.3^{+3.9}_{-2.7} \times 10^{-21}$	177.6*	–	0.67
	iNFW	$1.3^{+15.9}_{-0.6} \times 10^{-25}$	$320.5^{+99.0}_{-230.1}$	–	–	–	–	0.70

$11.48^{+0.00}_{-3.42} \times 10^{14} M_\odot$ for clusters MACS J0242 and MACS J0949 respectively. With equation (26), we find temperature normalisations $T_0 = \eta_T T_{500} = 7.30 \text{ keV}$ and 11.63 keV respectively.

Given the quality of the X-ray and SZ observations, and the dominant importance of the DMH and BCG in strong lensing models, we neglect the potentials associated to the individual galaxies, owing to the dynamical state of the clusters, analysed in Allingham et al. (2023). As they are not strongly perturbed, the ICM distribution should be governed by the large-scale potential. In Fig. 1, we can for instance see cluster MACS J0949 Southern halo mass contours to be undetectable on the X-rays – see the large red circle in the South of the image, crossed by the dashed green line.

Moreover, we postulate that the ICM density distribution is ellipsoidally symmetric, and of the same ellipticity as the DMH potential. This simply follows the hypothesis ‘ICM traces potential’. Therefore, as a natural consequence of the hydrostatic equilibrium, we expect the potential to be rounder than the total matter distribution (this is qualitatively verified on Fig. 1, and the potential ellipticity formula is presented in Appendix A).

Finally, as the line-of-sight ellipticity of the potential is assumed to be equal to the geometric average of the semi-major and semi-minor axes, \sqrt{ab} . As the goal of this article is to present new methods to predict the density profile of the ICM using strong lensing analyses, we fix all geometric parameters to their best lensing values. The ‘semi-depth’ of the cluster is unknown from lensing, but it is also degenerate with the density distribution. Therefore, we do not optimise this parameter.

6.6 MCMC optimisations

For the two different types of models of the electron density – canonical and analytical – represented by three different models – β , idPIE and iNFW – we let a number of parameters free. For the β profile, we set all three parameters of the density distribution $\{\rho_0; r_c; \beta\}$ free. For the idPIE profile, we initially let $\{\rho_{0,1}; a_1; s_1; \rho_{0,2}; s_2\}$ free, but as discussed in Sect. 7, s_2 appears entirely degenerate in the optimisation, and we therefore fix it to its lensing value. The two parameters characterising a NFW distribution, $\{\rho_S; r_S\}$, are set free for the iNFW optimisation. We optimise them with the data for each galaxy cluster. For cluster MACS J0242, we only use the X-ray data,

while for MACS J0949, we have the choice to use either X-rays, SZ, or both.

We define the log-likelihood for the X-ray data. As the photon counts are limited, the X-ray maps are following a Poissonian distribution. We take them to follow the Cash statistic (Cash 1979):

$$\ln \mathcal{L}_X(\Theta) = \frac{1}{N_X} \sum_i \left[C_i - M_i(\Theta) - C_i \ln \left(\frac{C_i}{M_i(\Theta)} \right) \right], \quad (33)$$

where $C_i = N_{X,c,i}$ is the data count in the i -th pixel (see eq. 30), N_X , the number of pixels, and $M_i(\Theta)$, the model prediction for the parameter vector, Θ .

As for the SZ statistic, with M_i now being the temperature contrast model, and C_i , its SZ measurement, we simply take the likelihood to be Gaussian:

$$\ln \mathcal{L}_{SZ}(\Theta) = -\frac{1}{2N_{SZ}} \sum_i \left[\left(\frac{M_i(\Theta) - C_i}{\sigma_i} \right)^2 + \ln \sigma_i^2 \right], \quad (34)$$

$$\sigma_i^2 = M_i^2(\Theta) + \sigma_{C,i}^2,$$

where σ_i is the standard deviation in the i -th pixel, and N_{SZ} , the number of SZ pixels. We take the model standard deviation to be the model itself, accordingly to a Gaussian model. $\sigma_{C,i}^2$ is the instrument variance of ACT. This does not take into account the CMB variance nor the atmosphere, but these are smoothed out on the scale of a cluster by the top-hat filtering (we follow Hilton et al. 2018, 2021). C_i and M_i represent here the data and model respectively, but for the SZ data. In the case of cluster MACS J0949, we sum the log-likelihood of the 90 and 150 GHz ACT DR5 bands.

In the case of the joint optimisation of X-rays and SZ, the data are of the same type, i.e. detections in pixels. We therefore define the joint likelihood as the weighted sum:

$$\ln \mathcal{L}_J = \frac{N_X \ln \mathcal{L}_X + N_{SZ} \ln \mathcal{L}_{SZ}}{N_X + N_{SZ}}, \quad (35)$$

where N_{SZ} must be understood as the sum of all SZ pixels, both in band f090 and f150. This takes into account the different pixelisations, and attributes equal weights to each pixel. The X-ray observations thus dominate, given the much better resolution (a *XMM-Newton* pixel represents $2.5''$, and an ACT pixel $30''$).

We used the package *emcee*, took 100 walkers, iterated over 5000

steps, with a step type `emcee.StretchMove`. We provide the cornerplots, realised with package `CORNER` (Foreman-Mackey 2016), in Appendix E.

7 ICM-OPTIMISED RESULTS

We present in this section the results of MCMC optimisations of each of the four ICM density models, for each galaxy cluster.

7.1 Cluster MACS J0242

7.1.1 β model

In order to compare our profiles inferred from lensing with the more popular profiles describing the ICM, we run a MCMC optimisation for the β profile. We present the optimised parameters in Table 4, alongside all other optimisations for MACS J0242. The associated cornerplot is presented Fig. E1.

We find the best likelihood to be $\ln \mathcal{L} = -0.68$, close enough from the best possible likelihood, -0.5 , so that we can expect other canonical ICM profiles – such as double- β – not to significantly improve the model.

7.1.2 *idPIE*

In the strong lensing optimisation – presented Table 2 – parameters $\{\rho_{0,1}; a_1; \rho_{0,2}; s_2\}$ were optimised, and the DMH cut radius, s_1 , to which strong lensing is insensitive, was fixed to 1.5 Mpc. Here, we optimise the *idPIE* density profiles with these density parameters using the *XMM-Newton* observations. We display both the strong lensing and ICM optimisations for the $\{\rho_{0,1}; a_1; s_1; \rho_{0,2}\}$ and $\{\rho_{0,1}; a_1; \rho_{0,2}\}$ parameter spaces in Fig. 6 and E2 respectively.

The X-ray optimisation of the BCG cut radius, s_2 , is degenerate (see Fig. E3). We therefore fix s_2 to its lensing value, $s_2 = 177.6$ kpc from now on. Although the prediction from lensing is diverging in the cluster centre ($r \rightarrow 0$) – due to the central matter density being out of the \mathcal{J}_z function bijective range – we find the ICM optimisation in the $\{\rho_{0,1}; a_1\}$ space to provide results in agreement with those from the lensing optimisation, despite the larger ICM error bars. The density normalisation of the BCG, $\rho_{0,2}$, yields different results than strong lensing. This may be explained by the high central matter density, which yields values out of the \mathcal{J}_z function inversion range. As the validity of equations (17) and (24) paired together is not verified beyond $n_e > 10^{-1} \text{ cm}^{-3}$, the ICM optimisation avoids regions of the parameter space yielding an ICM density above this value. Moreover, since the X-ray signal in the centre carries a high variability, we can not conclude about its significance.

We note that fixing the parameter s_1 to a value of 1.5 Mpc in the ICM optimisation results in a best log-likelihood $\ln \mathcal{L} < -1.06$. On the contrary, when this parameter is optimised, the best value gets closer to the ‘perfect fit’ -0.5 value at $\ln \mathcal{L} < -0.67$ (i.e. as good as the β model). In this case, we can only notice the X-ray optimisation is bound to diverge from the fiducial 1.5 Mpc value, as the best optimisation yields $s_1 = 2.72^{+0.44}_{-0.87}$ Mpc. The electronic densities, n_e , are represented in Fig. 7, and the *XMM-Newton* physical – i.e. without PSF effects – X-ray surface brightness, S_X , in Fig. 8. If s_1 is not optimised, we notice a discrepancy between the ICM best-fit and X-ray data profile at large radii ($R > 200$ kpc). This emphasises the necessity to let this parameter free. We conclude our method can properly fit the X-ray signal for this cluster, provided the potential is optimised, and notably s_1 . We further discuss the the importance of

s_1 and the large discrepancy between the lensing-inferred model and the observations in Sect. 7.3.

We can moreover outline the much larger error bars in the ICM optimisation, compared to the lens optimisation, in Fig. 6. This is due to the inherent difference in the data quality. The high sensitivity of the \mathcal{J}_z function (represented in Fig. 3) could be described as a double-edged sword: on the one edge, this sensitivity means any imprecision in the determination of the parameters, or even in the hypotheses (temperature model, temperature normalisation, determination of the total mass density, etc.) would result into a magnified error, i.e. a prediction error on the ICM density much larger than the total matter density associated error. On the other edge, this allows to finely tune certain parameters. In order to reach such a quality in the reconstruction, the strong lensing parameters should be very finely determined, and fixed. The parameters not fit with strong lensing (s_1 here) could then be optimised.

7.1.3 *inFW*

The NFW distributions attributed to strong lensing are all reductions of dPIE `LENSTOOL` optimisations to NFW best fit. In Fig. E4, we compare these to the ICM-optimised *inFW* parameters. The latter yields a very satisfactory best likelihood value again at $\ln \mathcal{L} = -0.70$, and although the $\{\rho_S; r_S\}$ values we find are different from those of the strong lensing reduction, they are compatible with the total density we found.

7.2 Cluster MACS J0949

Similarly to the study performed on the cluster MACS J0242, we present the results of the ICM optimisation of MACS J0949. We primarily present the joint fit results (X-rays and SZ effect).

7.2.1 β model

Figure E5 presents the optimisation with the ICM data from *XMM-Newton* and the SZ data taken with ACT. Using both the X-rays and SZ data for this optimisation, we find the best likelihood to be $\ln \mathcal{L}_J = -0.61$, a value which supports the good quality of the fit. In detail, the X-ray likelihood is $\ln \mathcal{L}_X = -0.58$, and the SZ likelihood is $\ln \mathcal{L}_{SZ} = -0.88$.

7.2.2 *idPIE*

As for MACS J0242, the optimisation of the BCG cut radius, s_2 , is degenerate. We therefore choose to fix this parameter to its strong lensing value, 98.0 kpc. We display in Fig. 9 the strong lensing and ICM optimisations in the $\{\rho_{0,1}; a_1; s_1; \rho_{0,2}\}$ parameter space. The best-fit value to the ICM data is $\ln \mathcal{L}_J = -0.60$. The overlap between the strong lensing and ICM optimised spaces is obvious in this cornerplot. However, the quality of the reconstruction with the ICM does not converge as efficiently as that of strong lensing – a result to be expected given the difference in methods and quality of data.

We present the comparison between the observations, the theoretical prediction using the lens model and the ICM-optimised model for observables, n_e , S_X , and Θ_r on Fig. 10, E7 and E8 respectively. Again, not optimising s_1 leads to a worst ICM optimisation (best log-likelihood -1.06 , see Fig. E6). In Fig. 10, the right panel shows the discrepancy between the X-rays inferred electron density and the best optimisation with a fixed DMH cut radius, $s_1 = 1.5$ Mpc. This

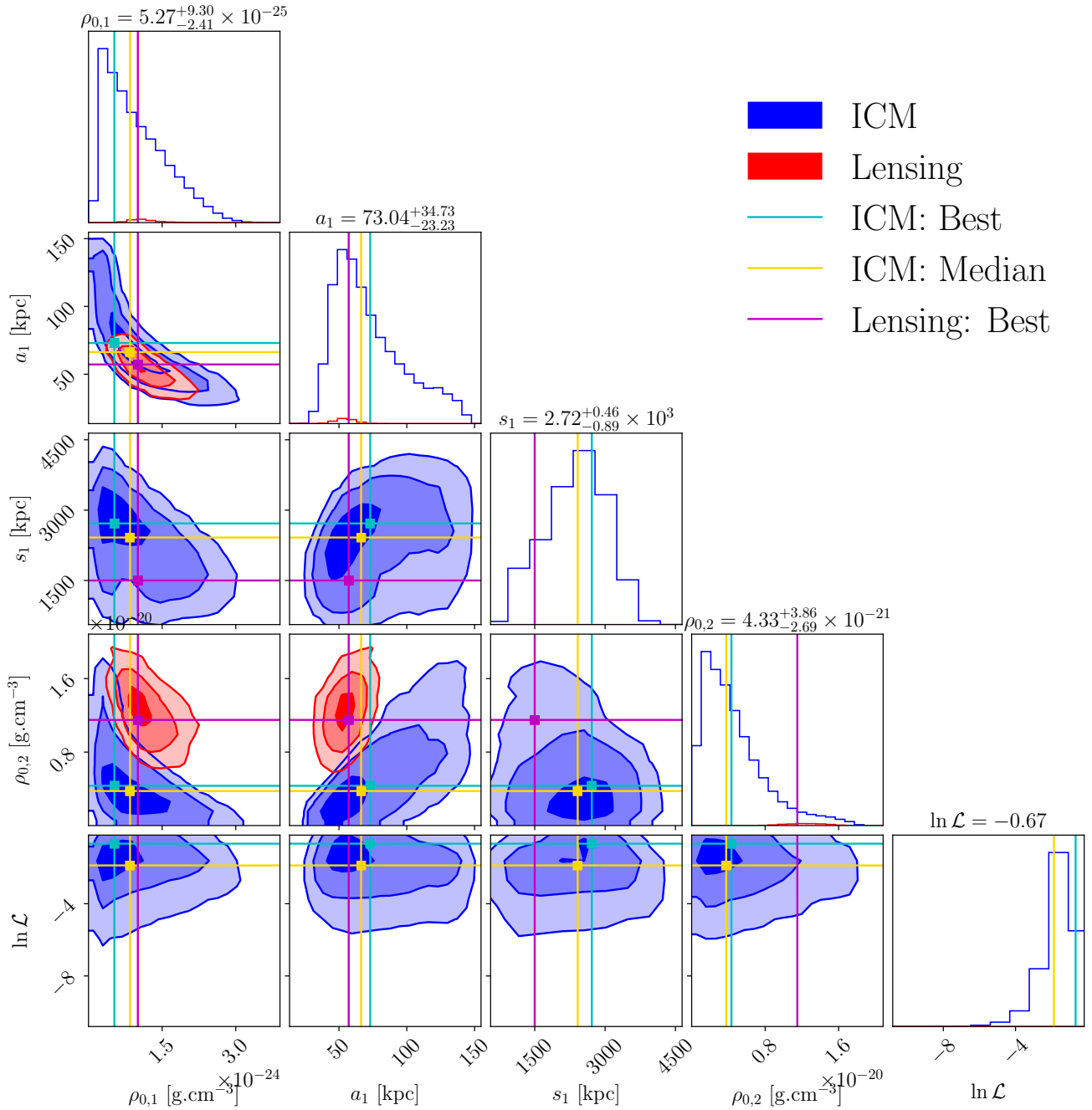


Figure 6. MCMC optimisation for idPIE model of the four relevant parameters for cluster MACSJ0242: DMH central density $\rho_{0,1}$ in g.cm^{-3} , core radius a_1 and cut radius s_1 in kpc, and BCG central density $\rho_{0,2}$ in g.cm^{-3} . *Blue*: Optimisation performed using the available ICM data (X-ray here). *Red*: Strong lensing optimisation. *Cyan*: Best-fit value of the ICM optimisation. *Gold*: Median ICM optimisation. *Magenta*: Best-fit strong lensing model (described in Table 2).

demonstrates the importance of this parameter optimisation to recover the X-ray measured density profile. We further discuss this in Sect. 7.3.

7.2.3 *iNFW*

In Fig. E9, we compare the best strong lensing optimisation fit to the ICM-optimised *iNFW* parameter space. We find a best log-likelihood

of $\ln \mathcal{L}_J = -0.61$. The strong lensing fit NFW parameters and the ICM-optimised values are compatible within 1σ .

7.3 Optimising the DMH cut radius with ICM core data and SL priors

As strong lensing is only efficiently probing the most central regions of galaxy clusters ($R < 200$ kpc), it only allows to effectively constrain the ‘central’ parameters amongst those presented in idPIE

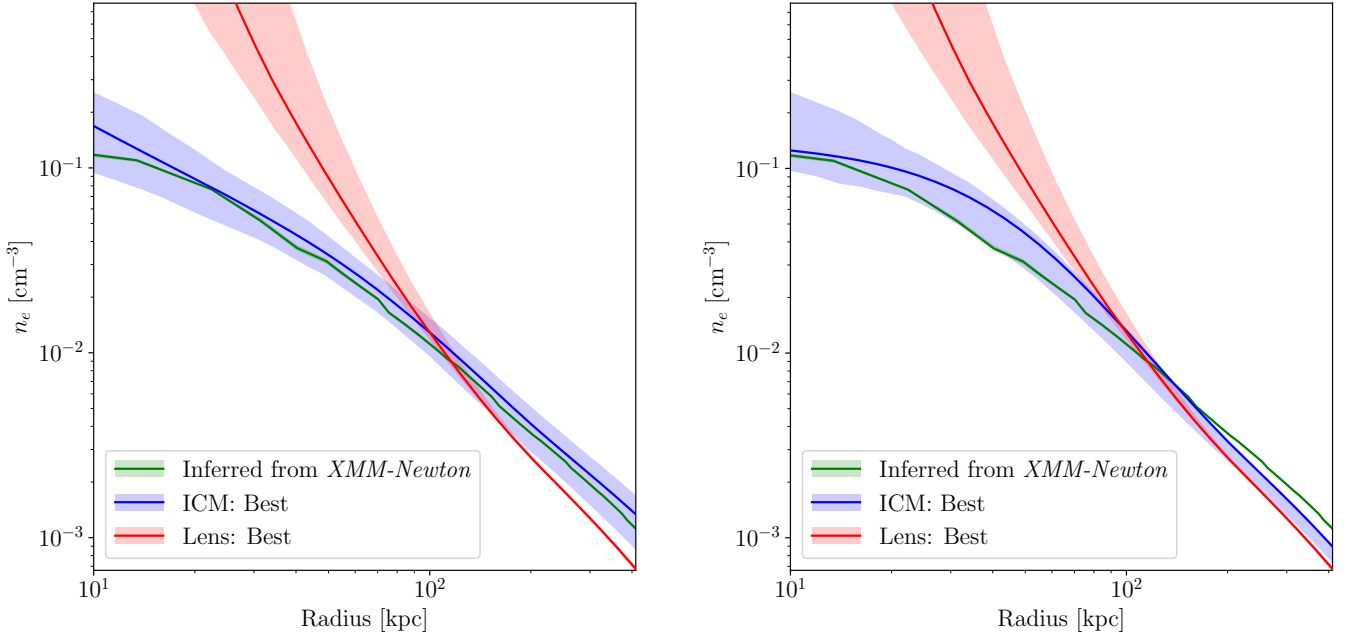


Figure 7. Electron density n_e for idPIE model, for cluster MACSJ0242. *Green*: X-ray surface brightness deprojected profile (assuming spherical symmetry). *Blue*: Best ICM-optimised profile, with an idPIE model. *Red*: Best lens model inferred profile. *Left*: In the case of the optimisation of parameters $\rho_{0,1}$, a_1 , s_1 and $\rho_{0,2}$, as illustrated in Fig. 6. *Right*: In the case of the optimisation of parameters $\rho_{0,1}$, a_1 and $\rho_{0,2}$, as illustrated in Fig. E2. This shows the lens-optimised ICM density model to be inconsistent with the X-ray data. As shown on Fig. 6, the X-ray optimised $\rho_{0,2}$ parameter yields lower values than the SL ones. This may be caused by ICM turbulence in the centre, or simply due to central total densities much larger than modelled through the polytropic temperature model (equation 24). More significantly, the offset in the ICM-optimised model on the right panel shows that if s_1 is not optimised, the larger scales (≥ 100 kpc) n_e densities can not be properly fitted.

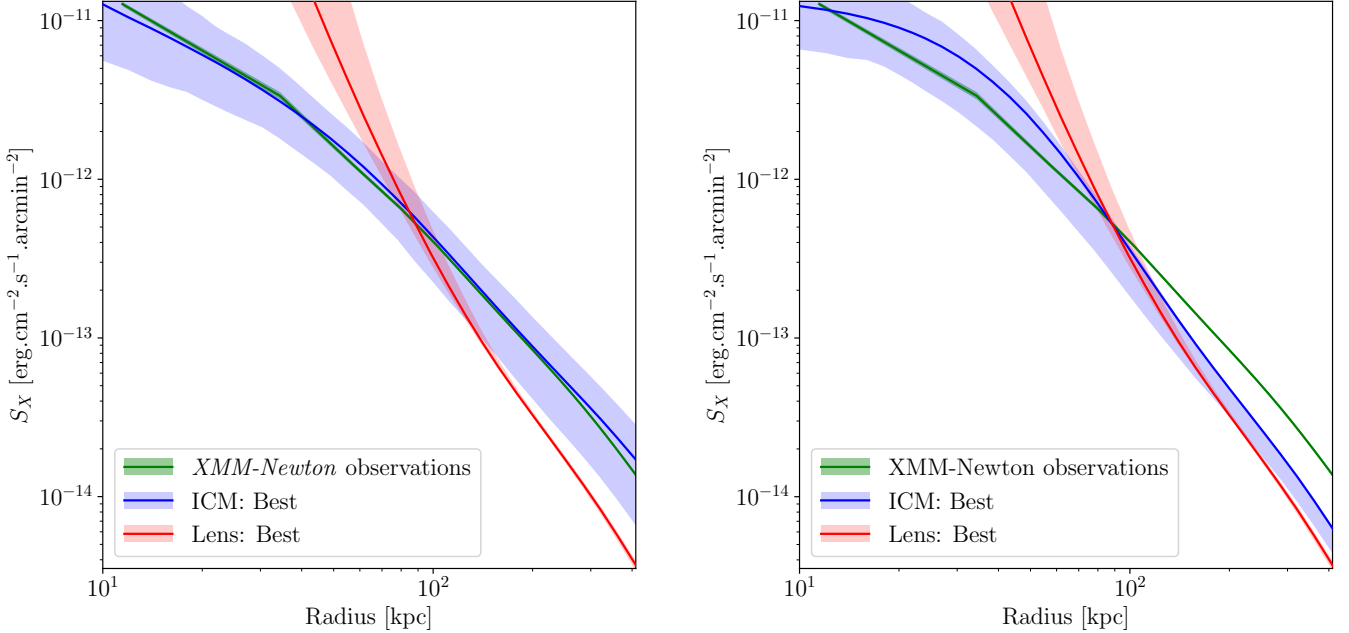


Figure 8. Expected X-ray surface brightness S_X for idPIE model, for cluster MACSJ0242. *Green*: X-ray surface brightness deprojected profile (assuming spherical symmetry). *Blue*: Best ICM-optimised profile, with an idPIE model. *Red*: Best lens model inferred profile. *Left*: In the case of the optimisation of parameters $\rho_{0,1}$, a_1 , s_1 and $\rho_{0,2}$, as illustrated in Fig. 6. *Right*: In the case of the optimisation of parameters $\rho_{0,1}$, a_1 and $\rho_{0,2}$, as illustrated in Fig. E2.

Table 5. Best fit of all optimisation models for cluster MACS J0949. The columns are as follows: (i) The observation type used to constrain the profile. (ii) The profile type. (iii) $\rho_{0,1}$ denotes the DMH central density in the case of idPIE profile, ρ_S in the iNFW case, and the central gas density ρ_c in the case of a β -profile. (iv) a_1 denotes the DMH core radius in the idPIE model, r_S the scale radius in the iNFW case, and r_c in the β -model. All of these distances are displayed in kpc. (v) s_1 denote respectively the cut radius of the DMH and of the BCG, in the case idPIE. (vi) $\rho_{0,2}$ denotes the BCG central density in the idPIE case. (vii) s_2 is the cut radius of the BCG. (viii) β is the power index of the β profile. (ix) $-\ln \mathcal{L}_J$ is the negative joint SZ-X-ray log-likelihood. The core radius of the BCG a_2 is model-dependent, and is thus it is not optimised here. Starred values were fixed.

Observation	Profile	$\rho_{0,1}, \rho_S$ or ρ_c	a_1, r_S or r_c	s_1	$\rho_{0,2}$	s_2	β	$-\ln \mathcal{L}_J$
Units		[g.cm ⁻³]	[kpc]	[kpc]	[g.cm ⁻³]	[kpc]		
Lensing	dPIE	$4.6^{+3.6}_{-1.0} \times 10^{-25}$	$116.3^{+24.1}_{-51.7}$	1500*	$3.9^{+8.3}_{-0.6} \times 10^{-18}$	$98.0^{+153.7}_{-34.3}$	–	3.54
	NFW	$1.2^{+1.6}_{-0.0} \times 10^{-25}$	$405.5^{+0.0}_{-156.1}$	–	–	–	–	1.42
ICM	β	$1.7^{+1.6}_{-1.0} \times 10^{-24}$	$108.4^{+175.0}_{-48.2}$	–	–	–	$0.50^{+0.28}_{-0.13}$	0.61
(X-rays and SZ)	idPIE	$3.6^{+8.2}_{-1.8} \times 10^{-25}$	$96.1^{+60.0}_{-32.6}$	3780^{+420}_{-1600}	$1.9^{+9.5}_{-1.1} \times 10^{-21}$	98.0*	–	0.60
	iNFW	$6.4^{+8.9}_{-2.1} \times 10^{-26}$	$546.2^{+110.3}_{-186.0}$	–	–	–	–	0.61

optimisations, i.e. $\rho_{0,1}, a_1, \rho_{0,2}$ and s_2 – leaving s_1 aside. Even these strong lensing constrained parameters are not perfectly determined in the case of our study as we are limited in the number of multiple images and spectroscopic redshifts detected (Allingham et al. 2023).

In this context, for the idPIE ICM optimisations, we notice the efficiency of the optimisation of the dark matter halo cut radius, s_1 . For MACS J0949⁷, we can use the idPIE model introduced in Sect. 7.2.2 and Fig. 9, and fix the parameters constrained through strong lensing, i.e. $\rho_{0,1}, a_1$ and $\rho_{0,2}$. This new model, only performing the s_1 -optimisation, reaches the best fit value, $s_1 = 3500^{+520}_{-740}$ kpc, at $\ln \mathcal{L}_J = -0.63$. This is much better than optimising all the other parameters excluding s_1 ($\ln \mathcal{L}_J = -1.06$). Thus optimising s_1 could suffice to fit the ICM density.

To verify this s_1 -optimisation does not affect the lens optimisation, we used the s_1 value for the best ICM optimisation of the idPIE model presented in Table 4 and 5 for respectively clusters MACS J0242 and J0949. Fixing the DMH cut radius to (respectively) 2720 and 3780 kpc, we perform a new lens optimisation for each cluster, following the procedure detailed in Allingham et al. (2023). We find that, for both clusters, this does not change significantly any of the optimised parameters. We find a close match between the respective *rms* of 0.37'' and 0.16'', compared to 0.39'' and 0.15'' *rms* with s_1 fixed to 1.5 Mpc. We conclude that using the ICM-optimised s_1 values does not strongly influence the strong lensing reconstruction.

8 DISCUSSION

8.1 Importance of the DMH cut radius

We remind the reader that the full idPIE ICM optimisation for clusters MACS J0242 and MACS J0949 respectively yielded $s_1 = 2720^{+440}_{-870}$ kpc and 3780^{+390}_{-1540} kpc – this latter value being compatible with the s_1 -optimisation only. Amongst all idPIE profile parameters, s_1 is the only one not to be optimised with strong gravitational lensing. Given the uncertainty in the determination of the lensing parameters due to observational limitations, the stiffness of function

\mathcal{J}_z^{-1} magnifies small errors in the potential profile into significant ones in the ICM density. Thus, these errors may contaminate the ICM-optimised s_1 value. If we could fix all other parameters (density parameters, geometry, and use a measured ICM temperature profile), the ICM-optimised value for s_1 should yield a physical result, with respect to the dPIE profile choice and the hydrostatic equilibrium hypothesis. In spite of this constraint on the data quality, we have presented the importance of the DMH cut radius parameter, s_1 , in the ICM density prediction, as its optimisation modifies the electron density, n_e , and thus the surface brightness, S_X , at all radii. Indeed, this DMH cut radius parameter, s_1 , is related to the total matter density in the cluster outskirts, but has a direct influence in the central X-ray surface brightness. This noticeable change in the ICM central density due to the s_1 DM halo cut radius is represented in Fig. E10. In the hydrostatic hypothesis, we can understand this as the effect of faster clustering of (baryonic) matter due to a larger dark matter halo, thus increasing the central baryonic density. In other words, if the gravitational potential at large radii is more important, a cluster should have accreted gas faster, and thus the ICM should be denser in the centre.

In order to securely compare the lens model to the ICM observables using the method presented in this article, future works should focus on relaxed, strong lensing galaxy clusters with a well-constrained lens model, including a large number of multiply-lensed systems. Given the utmost importance to know the limits of strong lens modelling (as demonstrated in e.g. Lin et al. 2023), one should not conclude on the dark matter halo properties without solid evidence. Moreover, weak lensing or a number of galaxy-galaxy strong lensing events far from the cluster centre should be coupled to the strong lens model, in order to lift the degeneracy on the potential constraints at large radii. In the settings of a similar parametric lens model as presented here, this would allow to constrain s_1 and to verify our optimisation results.

We may compare the cut radius to the *splashback radius*. This radius is defined as the largest distance from the cluster centre connected to the cluster dynamics, i.e. the largest orbital apocentre at which matter is accreted to the DMH. The cut radius values we find are larger than splashback radii measured by Chang et al. (2018). Their typical values provided in a redshift range corresponding to our lensing clusters are in the 1.5 – 2 Mpc range. These values are averaged for clusters of typical mass $M_{200,m} \approx 2.5 \times 10^{14} M_\odot$, to compare to the (extrapolated) 5.6 and $10.4 \times 10^{14} M_\odot$ for MACS J0242 and

⁷ For MACS J0242, we did not perform this optimisation, as the central pixels present a total density out of the invertible range of function \mathcal{J}_z , and optimising s_1 only would not suffice to bring the central density into the invertible range.

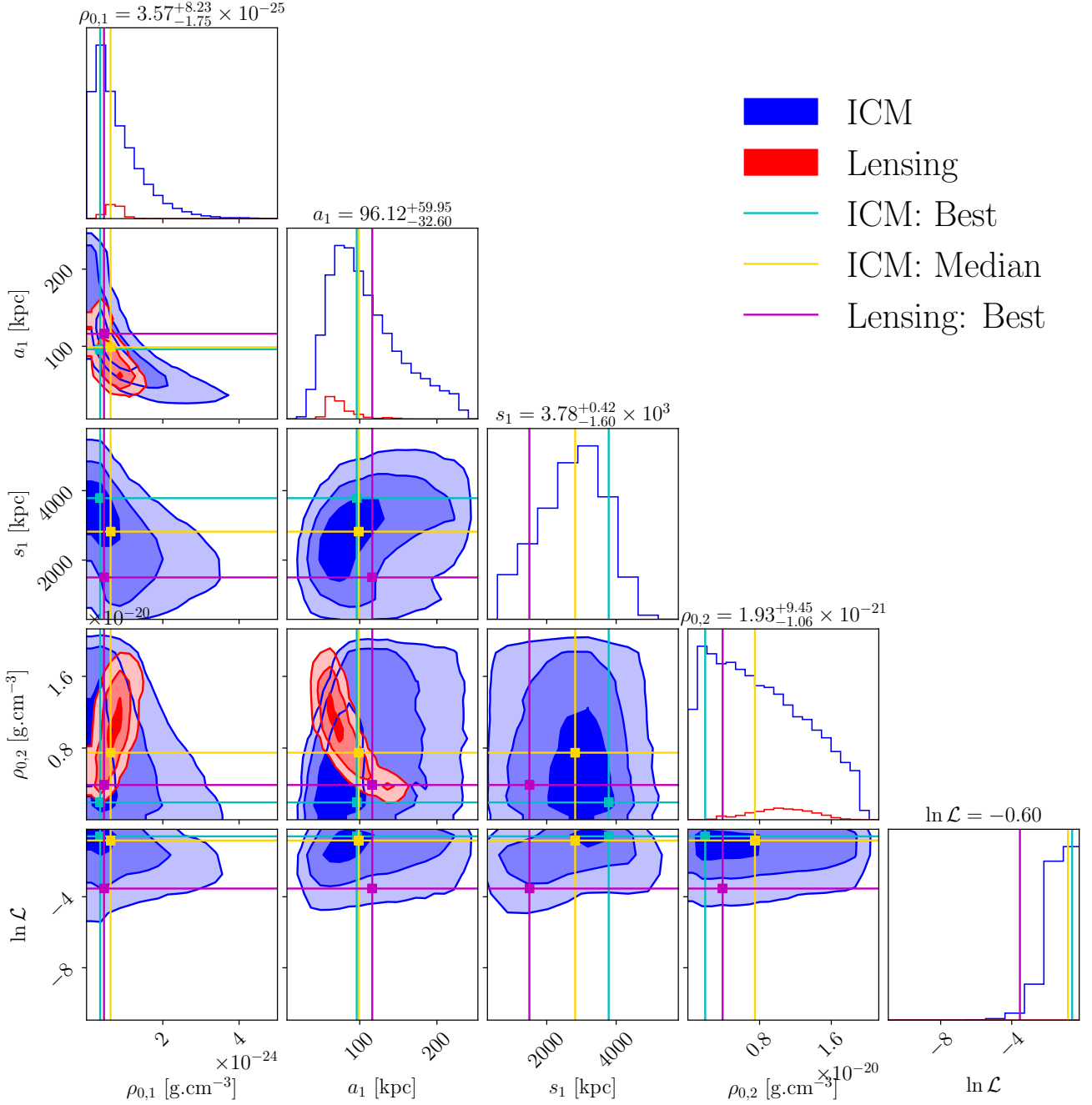


Figure 9. MCMC optimisation for idPIE model of the four relevant parameters for cluster MACSJ0949: DMH central density $\rho_{0,1}$, core radius a_1 and cut radius s_1 , and BCG central density $\rho_{0,2}$. The optimisation was performed with the X-ray and SZ data. *Blue*: Optimisation performed using the available ICM data. *Red*: Strong lensing optimisation. *Cyan*: Best ICM optimisation. *Gold*: Median of the ICM optimisation. *Magenta*: Best strong lensing model (described in Table 2).

MACSJ0949 respectively. As we expect more massive clusters to be larger, we do not find any contradiction to our s_1 values in this broad comparison. For a more quantitative assessment, we compare the logarithmic derivatives of the dPIE radial densities to the Diemer & Kravtsov (2014) density profiles (hereafter DK14). We find the transition between a logarithmic derivative of -2 to -4 to occur for the dPIE profile (with an optimised s_1 cut radius) from $0.5R_{\text{vir}}$ to $\sim 5R_{\text{vir}}$. This is in clear opposition to the DK14 predictions, for

which the heaviest clusters present a steepening of the derivative (see Fig. 2), and reaches a -4 logarithmic derivative for $\sim R_{\text{vir}}$.

We can also compare the cut radii obtained to the predicted *edge radius*, defined as the smallest radius at which no more orbiting galaxies can be found. According to Tomooka et al. (2020); Aung et al. (2023), the edge radius can be approximated to $r_e \sim 2R_{200,m}$. Using the ICM-optimised values for $R_{200,m}$, we can compare the optimised cut radius values to the edge radii for both clusters. We obtain for

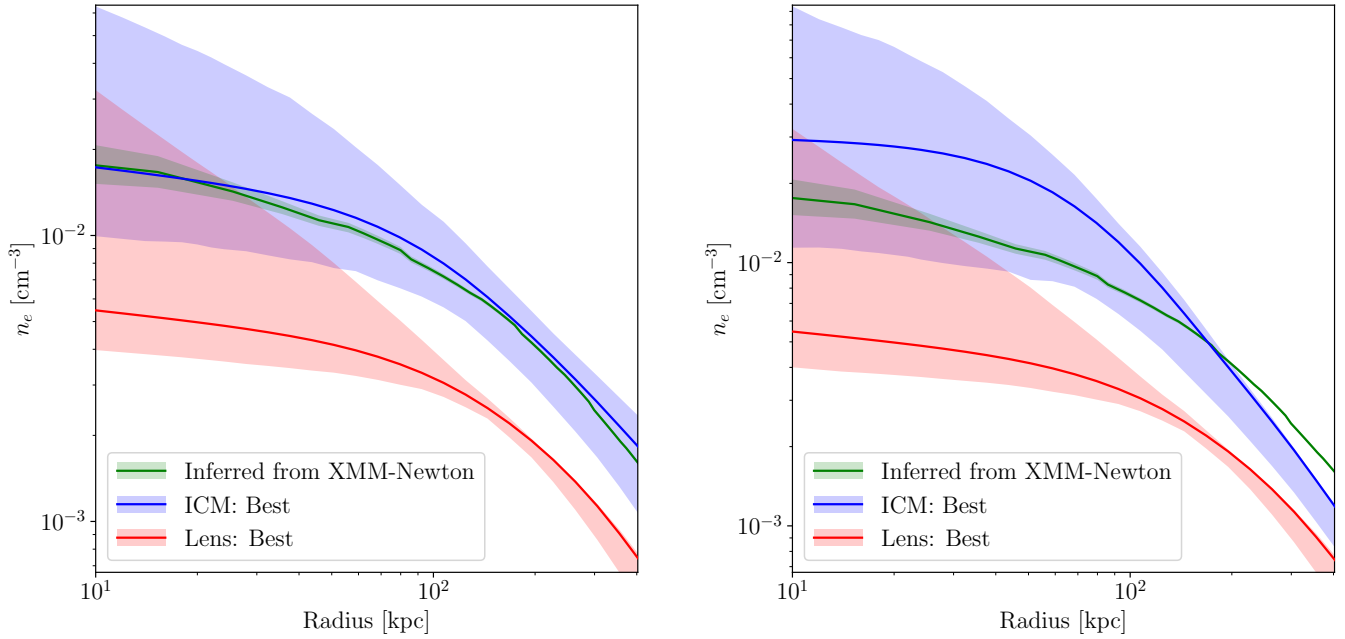


Figure 10. Electron density n_e for i dPIE model, for cluster MACS J0949. *Green:* X-ray surface brightness deprojected profile (assuming spherical symmetry). *Blue:* Best ICM-optimised profile, with an i dPIE model. *Red:* Best lens model inferred profile. *Left:* In the case of the optimisation of parameters $\rho_{0,1}$, a_1 , s_1 and $\rho_{0,2}$, as illustrated in Fig. 9. *Right:* In the case of the optimisation of parameters $\rho_{0,1}$, a_1 and $\rho_{0,2}$, as illustrated in Fig. E6. Similarly to Fig. 7, we observe that not optimising s_1 prevents our i dPIE model to fit the ICM density properly for $r \gtrsim 200$ kpc.

MACS J0242, $s_1 = 2720^{+440}_{-870}$ and $2R_{200,m} = 4632$ kpc. In the case of MACS J0949, we measure $s_1 = 3780^{+390}_{-1540}$ and $2R_{200,m} = 4751$ kpc. Computing the ratios $s_1/r_e = 0.59$ and 0.80 for the two clusters respectively, we obtain values of the same order. It should be noted that the cut, splashback and edge radii are not necessarily assumed to describe the same physical limit. As MACS J0242 presents a more cored profile than MACS J0949, we expect a higher DM concentration in the cluster centre. As a consequence, for a comparable bounded mass (e.g. $M_{200,m}$), we expect a lower s_1 value. This is compatible with the smaller s_1/r_e ratio found here. This serves to illustrate that, although of comparable orders of magnitude, s_1 and r_e do not exactly represent the same physical observables. The shock radius, describing the size of a shock of gas falling into the ICM of a cluster, is predicted by Baxter et al. (2021) to be equally of order $\sim 2R_{200,m}$, using SZ profiles issued from the Three Hundred Project hydrodynamic simulations. Although not quite observable with the ACT resolution, future SZ surveys will be able to assist detecting this critical ICM large scale cluster radius. We conclude that the optimised cut radii is commensurable to these various radii attempting to measure the ‘size’ of galaxy clusters, and we find s_1 to fall between the splashback and the edge radii. Using our analytical model, the thorough comparison of these different cluster-size radii should be greatly assisted by the combination of strong lensing and ICM observations.

8.2 ICM and DMH geometries

In order to understand the effect of the density profile parameters optimisation, one must decorrelate these from the geometric differences between the DMH and the ICM. Our measurements suggest that the ICM presents rounder shapes than the DMH (see e.g. Fig. 1). Indeed, in the case of clusters MACS J0242 and MACS J0949, the X-ray measured ellipticities are negligible, but the strong lensing op-

timisation of the DMH presents ellipticities in the range $0.2 - 0.3$. As studied in e.g. Debattista et al. (2008); Lau et al. (2012), the geometry of the ICM of (relaxed) galaxy clusters may differ from that of their DMH. Beyond baryonic effects associated to the ICM, the inability of CDM to dissipate kinetic energy tends to favour more elliptical DMH. According to Lau et al. (2011), simulations show both fluids’ ellipticity also varies importantly depending on the radius in which it is measured. As the ICM ellipticity is measured in a significantly larger radius, it is expected to be smaller. In this article, we modelled the ICM ellipticity to be that of the DMH measured through strong lensing. Any attempt to optimise the ICM density with spherical profiles yielded equivalent density profile parameters (ρ_0 , a , s) and best-fit likelihoods as using an elliptical profile (for both clusters, the Mahalanobis distance between the best-optimisations is of 0.3σ , and the $\ln \mathcal{L}$ difference < 0.01).

At last, line-of-sight projection effects were entirely neglected in this paper, and in the strong lensing reconstruction. The combination of SZ effect and X-ray observations may allow to inform asymmetries on the line-of-sight. However, given the SZ effect data resolution and the adoption of a self-similar temperature profile in this work, this is beyond the scope of this article. Such effects may nonetheless affect the quality of the reconstruction. For instance, Umetsu et al. (2015) display a case of apparent mismatch between ICM and lensing observations due to the presence of a line-of-sight asymmetry.

8.3 Relationship between DM and ICM densities

A number of additional observational effects limit the analytical ICM density reconstruction method. In general, relaxed galaxy clusters are expected to present a cool core, due to the radiated power in X-rays at high ICM densities. However, the observed central temperatures tend to be higher than the expected values considering only X-ray cooling (Peterson et al. 2001; Böhringer et al. 2002). This is gener-

ally explained by feedback effects, and most notably active galaxy nuclei (AGN, see e.g. Puchwein et al. 2010) and the cooling of the plasma. The change produced in the temperature profile was here taken into account by using the varying index, self-similar polytropic temperature model, which represents the physically measured temperatures, without implementing AGN feedback itself. However, this self-similar model is imperfect to take into account the feedback specific to each cluster. This may decorrelate the central ICM density from the DM in the outskirts. For instance, Ghirardini et al. (2019a, Fig. 7) present up to a 70% intrinsic scatter in the central density. The inclusion of a theoretical model for such baryonic effects would represent an important improvement to our models. Modelling the ICM fluid velocity evolution would also allow to understand the evolution of clusters, thus challenging the hydrostatic hypothesis.

Nevertheless, with precise lensing constraints and temperature model measurements in a cluster, we could directly compare the ICM data to the parametric lensing reconstruction, given our analytical models. The difference between the observations and the model, with respect to systematic errors, could yield constraints on the ICM velocity field and on dark matter models.

9 CONCLUSION

Using a comparison between a parametric strong lensing mass reconstruction model and the ICM observations (X-rays and SZ) on two non-perturbed galaxy clusters, we have shown it is possible to use a unique model to describe both the total and ICM density profiles. In fact, under the hydrostatic hypothesis and assuming self-similar electron temperature profiles, the bijection \mathcal{J}_z (equation 12) we have established between the total matter density and the ICM density allows to describe both the electron and dark matter density with the same parameters. We applied this technique to the dPIE and NFW potentials, and convincingly found the parameters optimised through lensing to be either compatible with their ICM optimisation, or to be degenerate and thus difficult to optimise with the ICM.

Given the sensitivity of this \mathcal{J}_z function, and as strong lensing does not allow to probe regions out of the cluster inner core, we paired our models to ICM observations. This allows to probe the *cut or scale radii* of relaxed clusters. Indeed, the ICM central density appears to be bounded to these matter density large-scale parameters. The method exposed in this article differs from traditional ways of accounting for ICM data in conjunction with strong lensing models, where the inferred gas potential is added to the lens model as a fixed (Paraficz et al. 2016; Bonamigo et al. 2017) or evolving (Beauchesne et al. 2024) component. Our new technique should be verified using clusters' outskirts surveys, such as weak lensing, and could only be efficiently applied with stringent constraints on the strong lensing parameters.

We can also reverse this perspective. If we had a perfect description of the full density mass model, e.g. including the cut radius of the DM halo through weak lensing, we could then compare the predicted ICM signal to that detected. If our model were satisfactory enough, we could then probe possible discrepancies, associated to other physical phenomena.

We here summarise the main results of this analysis:

1. We have proposed a self-similar polytropic temperature model with a varying index, using the X-COP sample of clusters. This allows to predict the ICM temperature for any cluster of measured mass $M_{500,c}$.

2. As a major result, we exhibited an *analytic* relationship between the ICM density and that of DM, assuming hydrostatic equilibrium.

We have further shown this relationship to allow to predict the ICM density using strong lensing, as a proof of concept.

3. We have demonstrated that the strong lensing ICM predictions are compatible with data through the ICM optimisation. We expect the strong lensing prediction to yield convincing results as long as: (i) the lensing galaxy cluster is not strongly perturbed, and (ii) we are able to properly predict the large-scale total density profile.

4. This requirement to probe the large scales demonstrates the limitations of our current analysis. We however foresee weak lensing constraints as a mitigating solution to adjust our models to large scale variations, thus allowing us to make precise predictions.

5. Reverting the perspective, this means the combination of X-rays or SZ data with strong lensing could allow to probe the dark matter profile of relaxed galaxy clusters far from their centres.

We have presented a proof of concept for the possibility to tie strong lensing constraints to the ICM. With higher-quality data and more observations on the large-scale profile, this should lead to powerful constraints on galaxy clusters physics.

Acknowledgements

The authors want to thank Alastair Edge, Jose Maria Diego and Benjamin Beauchesne for fruitful discussions. JA is supported by the Postgraduate Research Scholarship in Astroparticle Physics/Cosmology in the University of Sydney. JA acknowledges support by the Israel Science Foundation (grant no. 2562/20) and by the Center of Excellence of the Israel Science Foundation (grant No. 1937/19). MJ and DL are supported by the United Kingdom Research and Innovation (UKRI) Future Leaders Fellowship (FLF), 'Using Cosmic Beasts to uncover the Nature of Dark Matter' (grant number MR/S017216/1). The authors acknowledge the Sydney Informatics Hub and the use of the University of Sydney high performance computing cluster, Artemis.

DATA AVAILABILITY

The lens models and the lensing-ICM optimisation programmes are available upon reasonable request to the corresponding author.

References

- Ade P. A. R., et al., 2016, *Astronomy & Astrophysics*, 594, A13
Allingham J. F. V., et al., 2023, *MNRAS*, 522, 1118
Angelinelli M., Ettori S., Dolag K., Vazza F., Ragagnin A., 2023, *A&A*, 675, A188
Arnaud M., Pratt G. W., Piffaretti R., Böhringer H., Croston J. H., Pointecouteau E., 2010, *A&A*, 517, A92
Asplund M., Grevesse N., Sauval A. J., Scott P., 2009, *ARA&A*, 47, 481
Aung H., Nagai D., Rozo E., Wolfe B., Adhikari S., 2023, *MNRAS*, 521, 3981
Baxter E. J., Adhikari S., Vega-Ferrero J., Cui W., Chang C., Jain B., Knebe A., 2021, *MNRAS*, 508, 1777
Beauchesne B., et al., 2024, *MNRAS*, 527, 3246
Bezanson R., et al., 2022, *arXiv e-prints*, p. arXiv:2212.04026
Biffi V., et al., 2016, *ApJ*, 827, 112
Böhringer H., Werner N., 2010, *A&ARv*, 18, 127
Böhringer H., Matsushita K., Churazov E., Ikebe Y., Chen Y., 2002, *A&A*, 382, 804
Bonamigo M., et al., 2017, *ApJ*, 842, 132
Borgani S., Finoguenov A., Kay S. T., Ponman T. J., Springel V., Tozzi P., Voit G. M., 2005, *MNRAS*, 361, 233

- Bryan G. L., Norman M. L., 1998, *ApJ*, **495**, 80
- Bulbul G. E., Hasler N., Bonamente M., Joy M., 2010, *ApJ*, **720**, 1038
- Buote D. A., Humphrey P. J., 2012, *MNRAS*, **421**, 1399
- Böhringer H., Chon G., Kronberg P. P., 2016, *Astronomy & Astrophysics*, **596**, A22
- CHEX-MATE Collaboration 2021, *A&A*, **650**, A104
- Capelo P. R., Coppi P. S., Natarajan P., 2012, *Monthly Notices of the Royal Astronomical Society*, **422**, 686–703
- Cardone V. F., Piedipalumbo E., Tortora C., 2005, *MNRAS*, **358**, 1325
- Cash W., 1979, *ApJ*, **228**, 939
- Cavaliere A., Fusco-Femiano R., 1976, *A&A*, **500**, 95
- Chang C., et al., 2018, *ApJ*, **864**, 83
- Debatista V. P., Moore B., Quinn T., Kazantzidis S., Maas R., Mayer L., Read J., Stadel J., 2008, *ApJ*, **681**, 1076
- Diemer B., Kravtsov A. V., 2014, *ApJ*, **789**, 1
- Eckert D., Ettori S., Pointecouteau E., Molendi S., Paltani S., Tchernin C., 2017, *Astronomische Nachrichten*, **338**, 293
- Eckert D., et al., 2019, *A&A*, **621**, A40
- Eckert D., Ettori S., Pointecouteau E., van der Burg R. F. J., Loubser S. I., 2022, *A&A*, **662**, A123
- Einasto J., 1965, *Trudy Astrofizicheskogo Instituta Alma-Ata*, **5**, 87
- Elíasdóttir Á., et al., 2007, arXiv e-prints, p. arXiv:0710.5636
- Ettori S., Donnarumma A., Pointecouteau E., Reiprich T. H., Giodini S., Lovisari L., Schmidt R. W., 2013, *Space Sci. Rev.*, **177**, 119
- Ettori S., et al., 2019, *A&A*, **621**, A39
- Faber S. M., Jackson R. E., 1976, *ApJ*, **204**, 668
- Foreman-Mackey D., 2016, *The Journal of Open Source Software*, **1**, 24
- Foreman-Mackey D., Hogg D. W., Lang D., Goodman J., 2013, *Publications of the Astronomical Society of the Pacific*, **125**, 306–312
- Foster A. R., Ji L., Smith R. K., Brickhouse N. S., 2012, *The Astrophysical Journal*, **756**, 128
- Frenk C. S., et al., 1999, *ApJ*, **525**, 554
- Ghirardini V., et al., 2019a, *A&A*, **621**, A41
- Ghirardini V., Ettori S., Eckert D., Molendi S., 2019b, *Astronomy & Astrophysics*, **627**, A19
- Hammer F., 1987, in Bergeron J., Kunth D., Rocca-Volmerange B., Tran Thanh Van J., eds, *High Redshift and Primeval Galaxies*. pp 467–473
- Hernquist L., 1990, *ApJ*, **356**, 359
- Hilton M., et al., 2018, *ApJS*, **235**, 20
- Hilton M., et al., 2021, *ApJS*, **253**, 3
- Hogan M. T., et al., 2015, *Monthly Notices of the Royal Astronomical Society*, **453**, 1223
- Jullo E., Kneib J. P., Limousin M., Elíasdóttir Á., Marshall P. J., Verdugo T., 2007, *New Journal of Physics*, **9**, 447
- Kaiser N., 1986, *MNRAS*, **222**, 323
- Kassiola A., Kovner I., 1993, *ApJ*, **417**, 450
- Keeton C. R., 2001, arXiv e-prints, pp astro-ph/0102341
- King I. R., 1966, *AJ*, **71**, 64
- Kneib J.-P., Natarajan P., 2011, *The Astronomy and Astrophysics Review*, **19**
- Komatsu E., Seljak U., 2001, *MNRAS*, **327**, 1353
- Konrad S., Majer C. L., Meyer S., Sarli E., Bartelmann M., 2013, *A&A*, **553**, A118
- Landau L. D., Lifshitz E. M., 1959, *Fluid mechanics*. Pergamon Press
- Lau E. T., Nagai D., Kravtsov A. V., Zentner A. R., 2011, *ApJ*, **734**, 93
- Lau E. T., Nagai D., Kravtsov A. V., Vikhlinin A., Zentner A. R., 2012, *ApJ*, **755**, 116
- Lilley E. J., Evans N. W., Sanders J. L., 2018, *MNRAS*, **476**, 2086
- Lin J., Wagner J., Griffiths R. E., 2023, *MNRAS*, **526**, 2776
- Lotz J. M., et al., 2017, *The Astrophysical Journal*, **837**, 97
- Mahdavi A., Hoekstra H., Babul A., Bildfell C., Jeltrema T., Henry J. P., 2013, *ApJ*, **767**, 116
- Mallaby-Kay M., et al., 2021, *ApJS*, **255**, 11
- McDonald M., et al., 2016, *ApJ*, **826**, 124
- Mostoghiu R., Knebe A., Cui W., Pearce F. R., Yepes G., Power C., Dave R., Arth A., 2019, *MNRAS*, **483**, 3390
- Naess S., et al., 2020, *J. Cosmology Astropart. Phys.*, **2020**, 046
- Navarro J. F., Frenk C. S., White S. D. M., 1996, *The Astrophysical Journal*, **462**, 563
- Nelson K., Lau E. T., Nagai D., Rudd D. H., Yu L., 2014, *ApJ*, **782**, 107
- Paraficz D., Kneib J. P., Richard J., Morandi A., Limousin M., Jullo E., Martinez J., 2016, *A&A*, **594**, A121
- Peterson J. R., et al., 2001, *A&A*, **365**, L104
- Puchwein E., Springel V., Sijacki D., Dolag K., 2010, *MNRAS*, **406**, 936
- Rephaeli Y., 1995, *ARA&A*, **33**, 541
- Retana-Montenegro E., van Hese E., Gentile G., Baes M., Frutos-Alfaro F., 2012, *A&A*, **540**, A70
- Roncadelli M., Galanti G., 2021, arXiv e-prints, p. arXiv:2109.13284
- Salvatier J., Wiecki T. V., Fonnesbeck C., 2016, PyMC3: Python probabilistic programming framework, *Astrophysics Source Code Library*, record ascl:1610.016 (ascl:1610.016)
- Sereno M., Ettori S., Umetsu K., Baldi A., 2013, *MNRAS*, **428**, 2241
- Sereno M., Ettori S., Meneghetti M., Sayers J., Umetsu K., Merten J., Chiu I. N., Zitrin A., 2017, *MNRAS*, **467**, 3801
- Soucail G., Mellier Y., Fort B., Mathez G., Cailloux M., 1988, *A&A*, **191**, L19
- Steinhardt C. L., et al., 2020, *The Astrophysical Journal Supplement Series*, **247**, 64
- Stock D., et al., 2015, *A&A*, **584**, A63
- Tchernin C., et al., 2018, *Astronomy & Astrophysics*, **614**, A38
- Tomooka P., Rozo E., Wagoner E. L., Aung H., Nagai D., Safonova S., 2020, *MNRAS*, **499**, 1291
- Trevisan M., Mamon G. A., Stalder D. H., 2017, *MNRAS*, **471**, L47
- Umetsu K., et al., 2015, *ApJ*, **806**, 207
- Vazza F., Angelinelli M., Jones T. W., Eckert D., Brüggem M., Brunetti G., Gheller C., 2018, *MNRAS*, **481**, L120
- Vikhlinin A., Kravtsov A., Forman W., Jones C., Markevitch M., Murray S. S., Van Speybroeck L., 2006, *The Astrophysical Journal*, **640**, 691–709
- Voit G. M., 2005, *Reviews of Modern Physics*, **77**, 207
- Wilms J., Allen A., McCray R., 2000, *ApJ*, **542**, 914
- Zaroubi S., Squires G., de Gasperis G., Evrard A. E., Hoffman Y., Silk J., 2001, *The Astrophysical Journal*, **561**, 600–620

APPENDIX A: ELLIPTICITIES

We define the mass ellipticity e as:

$$e = \frac{a^2 - b^2}{a^2 + b^2}, \quad (\text{A1})$$

where a and b are the semi-major and semi-minor axes respectively.

Due to the Poisson equation, the ellipticity of the gravitational potential, i.e. here that of the ICM, differs from that of the mass ellipticity⁸:

$$\mathcal{E} = \frac{1 - \sqrt{1 - e^2}}{e} = \frac{a - b}{a + b}. \quad (\text{A2})$$

Upon defining an ellipsoidal radius, in order to take into account the potential ellipticity, assuming the ellipticity to be e , we take it to be:

$$r = \sqrt{\left(\frac{x \cos \theta + y \sin \theta}{a}\right)^2 + \left(\frac{y \cos \theta - x \sin \theta}{b}\right)^2 + \left(\frac{z}{c}\right)^2}, \quad (\text{A3})$$

in the Cartesian coordinates, with θ the rotation angle on the sky plane. c is the semi-axis along the line-of-sight, which we take to be the geometric average of a and b here.

⁸ This convention is provided by Kassiola & Kovner (1993). We tested it in practice, and we find this relationship to be appropriate, but it must be multiplied by a factor $\sqrt{2}$ when the ellipticity of the potential is measured in a 2D plane.

APPENDIX B: ALTERNATIVE DENSITY DISTRIBUTIONS

Beyond the NFW and dPIE density distributions, presented in Section 4.1, alternative models may be used to compute the ICM thermodynamic parameters using relationship (13).

B1 Generalised Navarro-Frenk-White profile

In the case of a generalised NFW potential (proposed as early as [Hernquist 1990](#)), we compute the different integrals given equation (6):

$$\begin{aligned} f(r) &= x^{-\gamma} (1+x^\alpha)^{-\frac{\beta-\gamma}{\alpha}}, \\ g(r) &= r_S^3 \frac{x^{3-\gamma}}{3-\gamma} {}_2F_1(\mu, \xi, 1+\mu, -x^\alpha), \\ h(r) &= r_S^2 \left\{ x^{2-\gamma} \left[\frac{{}_2F_1(\nu, \xi, 1+\nu, -x^\alpha)}{2-\gamma} \right. \right. \\ &\quad \left. \left. - \frac{{}_2F_1(\mu, \xi, 1+\mu, -x^\alpha)}{3-\gamma} \right] - \frac{\Gamma(\nu)\Gamma(\xi-\nu)}{\alpha\Gamma(\xi)} \right\}, \end{aligned} \quad (\text{B1})$$

where $x = r/r_S$, ${}_2F_1$ is the Gauss hypergeometric function, Γ the extended factorial function (i.e. the complete gamma function), and μ , ν and ξ are simple reformulations of the three indices α , β , γ :

$$\mu = \frac{3-\gamma}{\alpha}; \quad \nu = \frac{2-\gamma}{\alpha}; \quad \xi = \frac{\beta-\gamma}{\alpha}. \quad (\text{B2})$$

This integration takes constants into account, but requires $\alpha > 0$, $\beta > 2$ and $\gamma < 2$. The generalised NFW density is normalised by ρ_S , similarly to NFW: $\rho_{\text{gNFW}}(r) = \rho_S f(r)$.

B2 Einasto profile

The Einasto potential was proposed in [Einasto \(1965\)](#). Following [Cardone et al. \(2005\)](#); [Retana-Montenegro et al. \(2012\)](#), the different functions equation (6) write:

$$\begin{aligned} f(r) &= \exp(-s^{n-1}), \\ g(r) &= l^3 n \left[\Gamma(3n) - \Gamma(3n, s^{n-1}) \right], \\ h(r) &= -\frac{nl^2}{s} \left[\Gamma(3n) - \Gamma(3n, s^{n-1}) + s\Gamma(2n, s^{n-1}) \right], \end{aligned} \quad (\text{B3})$$

where n is the inverse index of the density slope at large radii, $s = (2n)^n r/r_{-2}$ the reduced scale radius, with r_{-2} a transition radius, $l = r_{-2}/(2n)^n$ the scale length and ρ_0 the central density. $\Gamma(\alpha)$ is the complete gamma function, and $\Gamma(\alpha, x)$ the incomplete upper gamma function:

$$\Gamma(\alpha, x) = \int_x^\infty dt t^{\alpha-1} e^{-t}. \quad (\text{B4})$$

The Einasto density writes $\rho_E(r) = \rho_0 f(r)$.

APPENDIX C: SELF-NORMALISED ICM DENSITY DISTRIBUTION

Following equation (11), assuming \mathcal{J} to be a bijection, we can also invert it and normalise the distribution at a given radius Δ (e.g. 100 kpc, where the strong lensing signal is strongly constraining the total density profile, or $R_{500,c}$), if we happen to know $n_{e,\Delta}$. We can therefore write:

$$n_e(r) = \mathcal{J}^{-1} \left[\mathcal{J}(n_{e,\Delta}) \frac{\Phi(r)}{\Phi(R_{\Delta,c})} \right]. \quad (\text{C1})$$

We call this latter expression *self-normalised*.

We did not include any self-normalised models in the optimisations, as these imply to use X-ray data both as input (as a normalisation) and to perform the optimisation, which would make one or several parameters degenerate.

APPENDIX D: GAS FRACTION STUDY

D1 Gas fraction definition

We define the gas fraction as the ratio of the gas mass to the total mass. The gas mass includes all baryons except stars. We distinguish the local gas fraction, $f_g(r) = \rho_g(r)/\rho_m(r)$, considered in this article to be a radial function, and the cumulative gas fraction, F_g , given within a radius r :

$$F_g(r) = \frac{\int_0^r ds s^2 \rho_g(s)}{\int_0^r ds s^2 \rho_m(s)} = \frac{M_g(<r)}{M_m(<r)}, \quad (\text{D1})$$

$$f_g(r) = \frac{dF_g}{dr}(r) \frac{\int_0^r ds s^2 \rho_m(s)}{r^2 \rho_m(r)} + F_g(r).$$

The full knowledge of either of these gas fractions would provide a bijective relationship between the gas and matter content of galaxy clusters. We will therefore name *gas density reconstruction* our electron density prediction using an empirical gas density model.

We here present an alternative attempt to model the hot gas distribution using the gravitational potential. Using the local gas fraction $f_g = \rho_g/\rho_m$, a general model for f_g coupled with the lensing constraints on ρ_m would yield a ρ_g prediction in each lensing cluster.

In order to derive a quantitative model for the gas fraction, we use the ‘X-COP+2’ sample analysis, i.e. the X-COP (*XMM* Cluster Outskirts Project) sample, complemented with similar analyses for our two strong-lensing clusters, MACS J0242 and MACS J0949. We compare the cumulative gas fraction reconstruction (as defined in eq. D1) in each of the 14 clusters in the sample, and propose two new *ad hoc* models.

D2 Proposed models

With respect to the data analysed in Sect. D3, we propose the following models. First, we attempt to describe the increasing cumulative gas fraction, F_g , as a power law:

$$F_g(r) = f_g^0 \left(1 + \frac{r}{r_c} \right)^\zeta, \quad (\text{D2})$$

where r_c is a pivot, or core radius, $f_g^0 = F_g(r=0)$, the central gas fraction, i.e. the baryonic fraction excepted the stellar fraction, and ζ , the power exponent to find.

However, for all clusters, the integrated gas fraction presents a transition between the inner and the outer regions of the cluster, as represented on [Eckert et al. \(2019, Fig. 1\)](#). We propose to analytically describe this transition with a *transitive* model:

$$F_g(r) = a \left[\frac{2}{\pi} \arctan \left(\exp \frac{r-r_c}{r_f} \right) - \frac{1}{2} \right] + b, \quad (\text{D3})$$

where a and b are defined with the expected gas fraction at two given radii, respectively at R_E , a radius where the potential is typically constrained through strong gravitational lensing (e.g. the Einstein radius), and at $R_{500,c}$, where the gas fraction should tend towards

the Universal gas fraction. We respectively write these gas fractions F_g^E and F_g^{500} :

$$\begin{aligned} \nu(r) &= \frac{2}{\pi} \arctan \left[\exp \left(\frac{r - r_c}{r_f} \right) \right], \\ a &= \frac{F_g^{500} - F_g^E}{\nu(R_{500}) - \nu(R_E)}, \\ b &= F_g^{500} - a\nu(R_{500}), \end{aligned} \quad (\text{D4})$$

and r_p and r_f are the pivot radius and flattening distance respectively, i.e. the radii of the transition inflexion point, and the characterisation of the slope of the transition.

In the simplest model, i.e. assuming a cluster to be dynamically relaxed, the local gas fraction pivot scale should be related to the pivot parameter in the total matter density ρ_m . For instance, in a NFW description, this parameter would be the scale radius r_S , as $f_g(r) = \rho_g(r; r_S) / \rho_m(r; r_S)$, using the hydrostatic relationship (13). Therefore, we can take a_1 , a typical BCG-to-DMH transition radius, to be a reasonable prior on both the pivot radius r_p and the flattening distance r_f . Important limitations nonetheless prevent from identifying these values to be identical. Indeed, multiple parametrisations of the typical pivot radius exist in the potential, and are not identical to a unique pivot scale. More importantly, the distribution of hot gas is dominated by non-gravitational phenomena (AGN feedback, plasma turbulence, etc.), whose characteristic radii have no *a priori* reason to match the potential's. For F_g^{500} , we assume $F_g^{500} \simeq f_g^{500}$, and we use the universal gas fraction $\Omega_b / \Omega_m = 0.1580 \pm 0.0021$ (Ade et al. 2016), corrected for the stellar fraction f_\star , not accounted for in the intracluster gas, and the baryon depletion factor Y_b (see Eckert et al. 2019):

$$f_g^{\text{th}}(r) = Y_b(r) \frac{\Omega_b}{\Omega_m} - f_\star(r). \quad (\text{D5})$$

Eckert et al. (2019) provide $Y_{b,500} = 0.938^{+0.028}_{-0.041}$, which we use here. Following the same study, we take the error on $f_{\star,500}$ to be 5×10^{-3} . The study of the lensing galaxy clusters gives stellar fraction of $f_{\star,500} = (1.92 \pm 0.21) \times 10^{-2}$ and $(1.87 \pm 0.36) \times 10^{-2}$ for MACS J0242 and J0949 respectively.

D3 X-COP+2 study

With the power-law and the transitive models, equations (D2) and (D3) respectively, we conduct a study for the 14 galaxy clusters of the X-COP+2 sample.

All these clusters were tested with both the power-law and transitive models, optimised for all respective 3 and 4 parameters ($\{f_g^0, r_c, \zeta\}$ and $\{F_g^E, F_g^{500}, r_p, r_f\}$) with a MCMC, with package EMCEE (see Foreman-Mackey et al. 2013). We arbitrarily took $R_E = 50$ kpc, as both lensing clusters present strong constraints in this region, and the gas fraction at this radius is significantly different from that at $R_{500,c}$ for all clusters. We define the log-likelihood function as Gaussian, with an underestimated variance of fractional amount, f :

$$\ln \mathcal{L}_{f_g}(\Theta) = -\frac{1}{2} \sum_i \left[\left(\frac{F_{g,i}^{\text{val}} - F_{g,i}^{\text{pred}}(\Theta)}{\sigma_i} \right)^2 + \ln \sigma_i^2 \right], \quad (\text{D6})$$

where $F_{g,i}^{\text{val}}$ are the values of the cumulative gas fraction in radius bins (the gas mass being measured through X-ray deprojection, and the total mass obtained using the hydrostatic equilibrium), $F_{g,i}^{\text{pred}}$ are

Table D1. Average over all clusters of the optimised parameters for the gas fraction power law model. r_c is in kpc.

f_g^0 (%)	r_c [kpc]	ζ
1.26 ± 1.12	1.01 ± 0.62	0.41 ± 0.14

Table D2. Average over all clusters of the optimised parameters for the gas fraction transitive model. r_p and r_f are in kpc.

F_g^E (%)	F_g^{500} (%)	r_p [kpc]	r_f [kpc]
5.59 ± 2.21	13.6 ± 2.1	20.4 ± 65.6	259.8 ± 135.8

the predictions in the same bins, and:

$$\sigma_i^2 = (\sigma_i^{\text{err}})^2 + \left[F_{g,i}^{\text{pred}}(\Theta) \right]^2 f^2, \quad (\text{D7})$$

where σ_i^{err} are the $F_{g,i}^{\text{val}}$ measured standard deviation error. In practice, the model scatter f is optimised.

Out of the 14 clusters, 5 were found to be better modelled with the power-law, and 9 with the transitive relationship – including MACS J0242 and MACS J0949. We performed the optimisation over all radii accessible in the X-ray data range, except for MACS J0242, where non-statistically significant perturbations exist in the gas fraction reconstruction. To avoid these, the optimisation was performed in $r \in [20; 350]$ kpc for this specific cluster.

Overall, we find the transitive model to be consistently better. Indeed, even the clusters which were better modelled by a power-law are well fit by a transitive model. The largest model scatter on the power-law model reaches $f = 17\%$, to be compared with the maximum of $f = 9\%$ for the transitive model. Moreover, by construction, the transitive model can use physical parameters as priors for F_g^{500} , r_p and r_f , and converges at large radii, which is expected from the Universal hot gas fraction. We give in Tables D1 and D2 the optimised parameters for respectively the power-law and the transitive models. These are the averages of the best parameters found by the MCMC for each individual cluster.

Trying to relate these parameters to physical values, we notice that f_g^0 is the gas fraction at the centre of the clusters. The X-COP+2 sample does not precisely provide the hot gas fraction in the centre of clusters ($r < 20$ kpc), due to the stellar effects, turbulence, feedback and resolution of X-ray surveys. For these reasons, we do not directly use a physically measurable value for f_g^0 , and simply use a fit of this parameter across all radii. Conversely, F_g^E is well measured for all the clusters of the sample, but we can not generalise this value overall.

The exponent ζ of the power-law model is purely empirical. As for the power-law pivot radius, r_c , its relative error bars are quite important. However, discarding the two clusters coming from lensing yields $r_c = 0.96 \pm 0.65$ kpc, i.e. a result very close the X-COP+2 one. The same process on ζ and f_g^0 gives results similar to those presented in Table D1, for respectively $\zeta = 0.41 \pm 0.14$ and $f_g^0 = (1.2 \pm 1.1) \times 10^{-2}$. We can therefore propose a model:

$$F_g(r) = 1.3 \times 10^{-2} \left[1 + \frac{r}{1.0 \text{ kpc}} \right]^{0.41}. \quad (\text{D8})$$

However, given the important error bars found on all parameters of this model, its inability to predict accurately the gas fraction for most

Table D3. Updated parameters and model for the gas fraction transitive model, for the X-COP clusters only. r_f is in kpc.

F_g^E (%)	F_g^{500} (%)	r_f [kpc]
5.40 ± 1.83	13.7 ± 1.9	290.7 ± 122.1

clusters, and the lack of theoretical motivation for its parameters, we conclude to the ineffectiveness of this model.

As for the transitive model, all parameters may be physically interpreted. The quantity F_g^{500} not only can be found quite precisely, but is also in agreement with equation (D5). Indeed, for all X-COP clusters, the stellar fraction is considered to be unknown. We could use the X-COP average value $f_{\star,500} = 0.015 \pm 0.005$, but prefer to use the results of simulations presented in Angelinelli et al. (2023). Given a M_{500} , which we have for X-COP clusters, we can draw a value for $f_{\star,500}$. Completing the set with the stellar fractions found in Allingham et al. (2023) for the lensing clusters, we can fix the F_g^{500} value for each cluster. These values are in remarkable agreement with Table D2. As for r_p and r_f , we can not study the X-COP clusters and our lensing clusters jointly. Indeed, we are using a_1 , the core radius of the DMH, as a prior on both these parameters. However this radius is unknown for the X-COP clusters due to the lack of lensing data. Moreover, the best fit values of r_p for the X-COP clusters are all < 2 kpc, while for MACS J0242, $r_p = 22.9^{+48.0}_{-16.2}$ kpc and for MACS J0949, $r_p = 256.1^{+16.7}_{-29.2}$ kpc.

Therefore, for the dynamically relaxed X-COP clusters, we can set $r_p = 0$. After performing an optimisation on the X-COP clusters only of this restricted model, we find the average best parameters summarised in Table D3. The largest model scatter across all 12 clusters is still of $f = 9\%$. If we chose to constrain F_g^{500} using eq. (D5), the largest f would be of 36%.

Given the results in the lensing clusters transitive model optimisation, we choose to fix r_p to the a_1 prior for both MACS J0242 and MACS J0949. This is an effective model, which should be further informed using observations on other lensing clusters. We then find the model error to be respectively $f = 1.7\%$ and 1.8% . On all 14 clusters, we may prolong the transitive function into a central gas fraction F_g^0 , which is predicted to be $F_g^0 = 2.6 \pm 1.9\%$, averaging on all clusters, with the fixed r_p models. We may thus fix all parameters (using formula D5 for F_g^{500}), except r_f . This final model is represented and compared to the transitive model with all parameters let free on Figure D1. We find a maximum scatter of $f = 40\%$, but the average scatter at 8.7% . As expected, the local models appear to be better fits, but we notice the reduced model (r_f free only displayed in blue is a good approximation (the X-ray reconstruction is never distant of more than 2σ from the ‘reduced’ models, in the fitting radii range). For the lensing clusters, we can not conclude on the scale to set for r_p , but found the approximation $r_p \approx a_1$ to be empirically reasonable. We can not conclude absolutely on the flattening distance r_f , with the final model yielding $r_f = 26.5^{+4.0}_{-2.8}$ kpc for MACS J0242 and $r_f = 267.3^{+19.9}_{-16.4}$ kpc for MACS J0949. A larger study would be necessary to conclude to the general validity of a reduced transitive model without any free parameter. For the X-COP clusters, r_f ranges from 80 to 750 kpc, and we can thus not conclude either. Studying the morphology and dynamical state parameters may allow to determine r_f using observable data.

As we could not extract a general, Universal prediction for the gas fraction simply using lensing-determined parameters, we can not conclude to the success of this technique for the moment. The

transitive model is however encouraging, and a more general study coupling X-ray and lensing data may manage to generalise the resisting parameter r_f .

APPENDIX E: CORNERPLOTS

We display here the cornerplots of the MCMC optimisations of the potential of the ICM data, as described Sect. 8. In the following graphs, densities ρ are displayed in g.cm^{-3} , while core, scale and cut radii in kpc.

This paper has been typeset from a $\text{\TeX}/\text{\LaTeX}$ file prepared by the author.

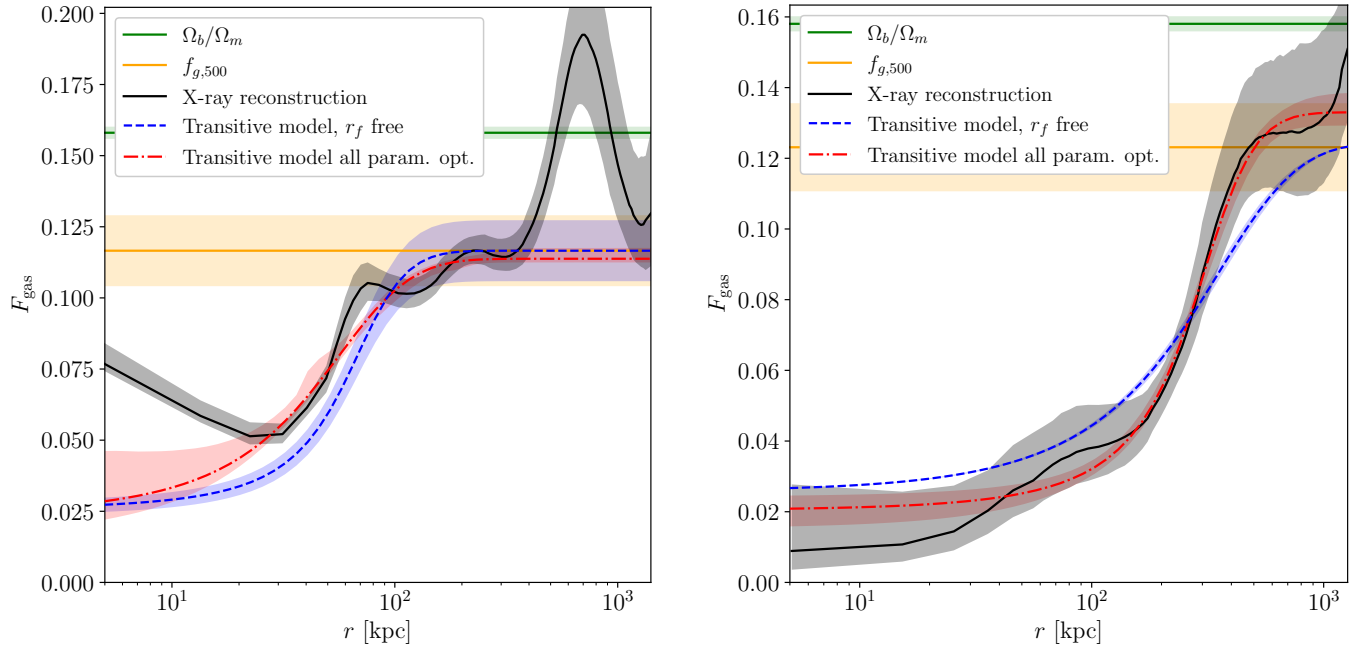


Figure D1. Cumulative gas fraction $F_g(r)$ in lensing galaxy clusters MACSJ0242 (left) and MACSJ0949 (right). *Black*: Reconstructed gas fraction from *XMM-Newton* data analysis. Errors are 1σ . *Green*: Universal gas fraction Ω_b/Ω_m . *Orange*: Gas fraction at $R_{500,c}$ (see eq. D5). *Red*: Transitive gas fraction model (see equation D3) optimised for the specific cluster. *Blue*: Transitive model with the cluster lensing parameter a_1 as r_D , and F_g^0 and F_g^{500} determined using the general reduction over X-COP+2 and the theoretical gas fraction f_g^{500} respectively. As presented in e.g. Eckert et al. (2022), the baryon fraction is approximately constant out of the central regions of clusters. Baryons are distributed between stars and the ICM, with a higher concentration of the former in the centre, and of the latter in the outskirts ($r > 0.2R_{500}$). This matches the trend presented here.

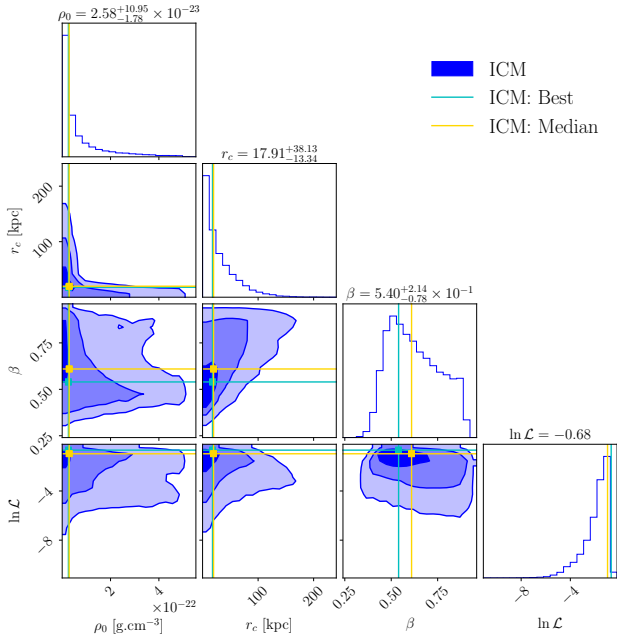


Figure E1. MCMC optimisation for β model of the three relevant parameters for cluster MACSJ0242: central density $\rho_{0,1}$, core radius r_c and density index β . As per all other cornerplots, the density $\rho_{0,1}$ is here displayed in g.cm^{-3} and the core radius r_c in kpc. *Blue*: Optimisation performed using the available ICM data (X-ray here). *Gold*: Median of the ICM optimisation. *Cyan*: Best ICM optimisation (described in Table 2). These best ICM-optimisation values are displayed over the histogramme distributions.

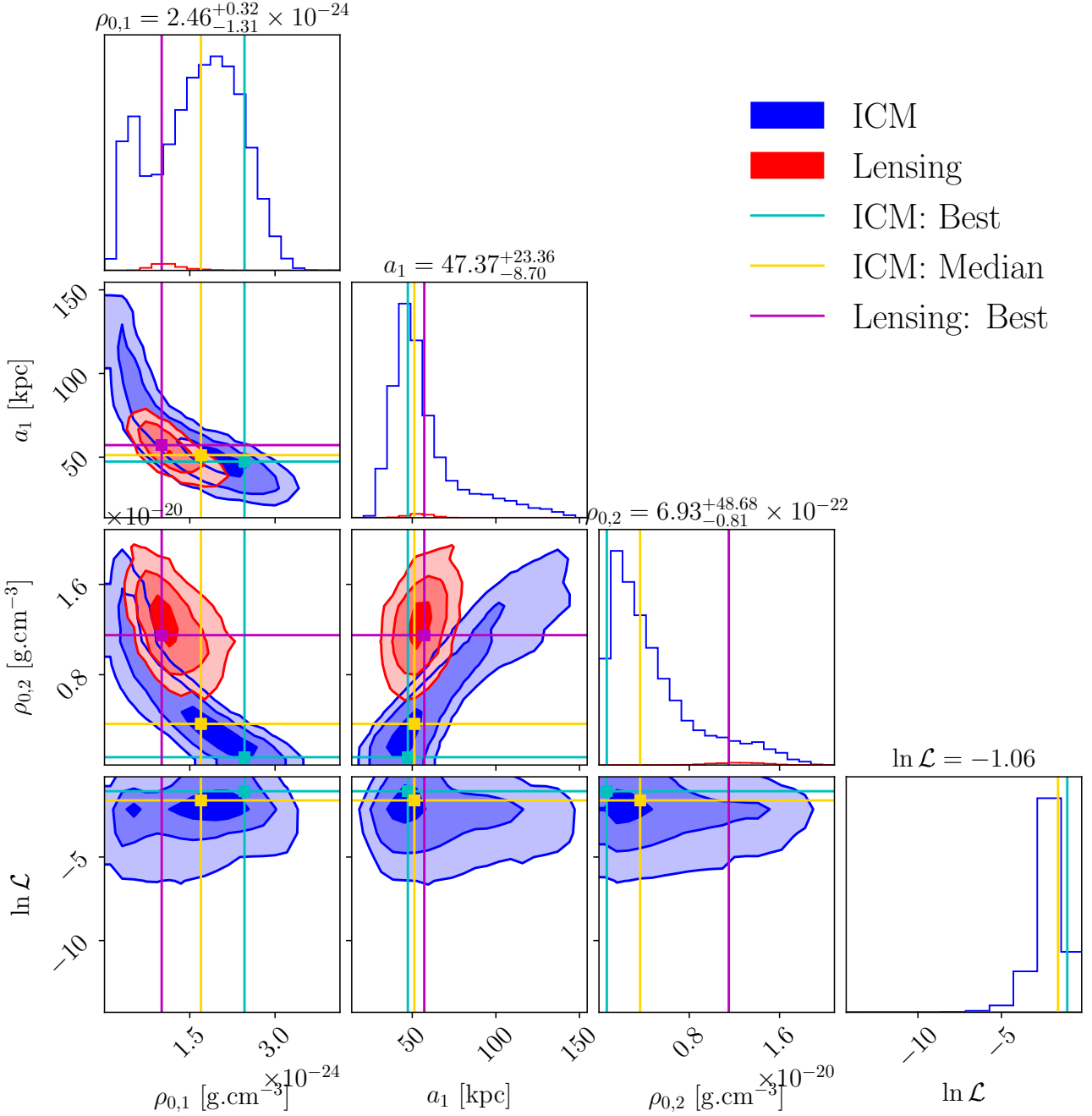


Figure E2. MCMC optimisation for idPIE model, for cluster MACSJ0242: DMH central density $\rho_{0,1}$ and core radius a_1 , and BCG central density $\rho_{0,2}$. The DMH cut radius is fixed to the fiducial value of 1.5 Mpc. Densities are displayed in g.cm^{-3} , distances in kpc. *Blue*: Optimisation performed using the available ICM data (X-ray here). *Red*: Strong lensing optimisation. *Cyan*: Best ICM optimisation. *Gold*: Median of the ICM optimisation. *Magenta*: Best strong lensing model (described in Table 2). Comparing this to Fig. 6, we notice the importance of the optimisation of parameter s_1 , as the ICM best-fit likelihood here is -1.06 , i.e. the optimisation is of much worse quality than with this optimisation.

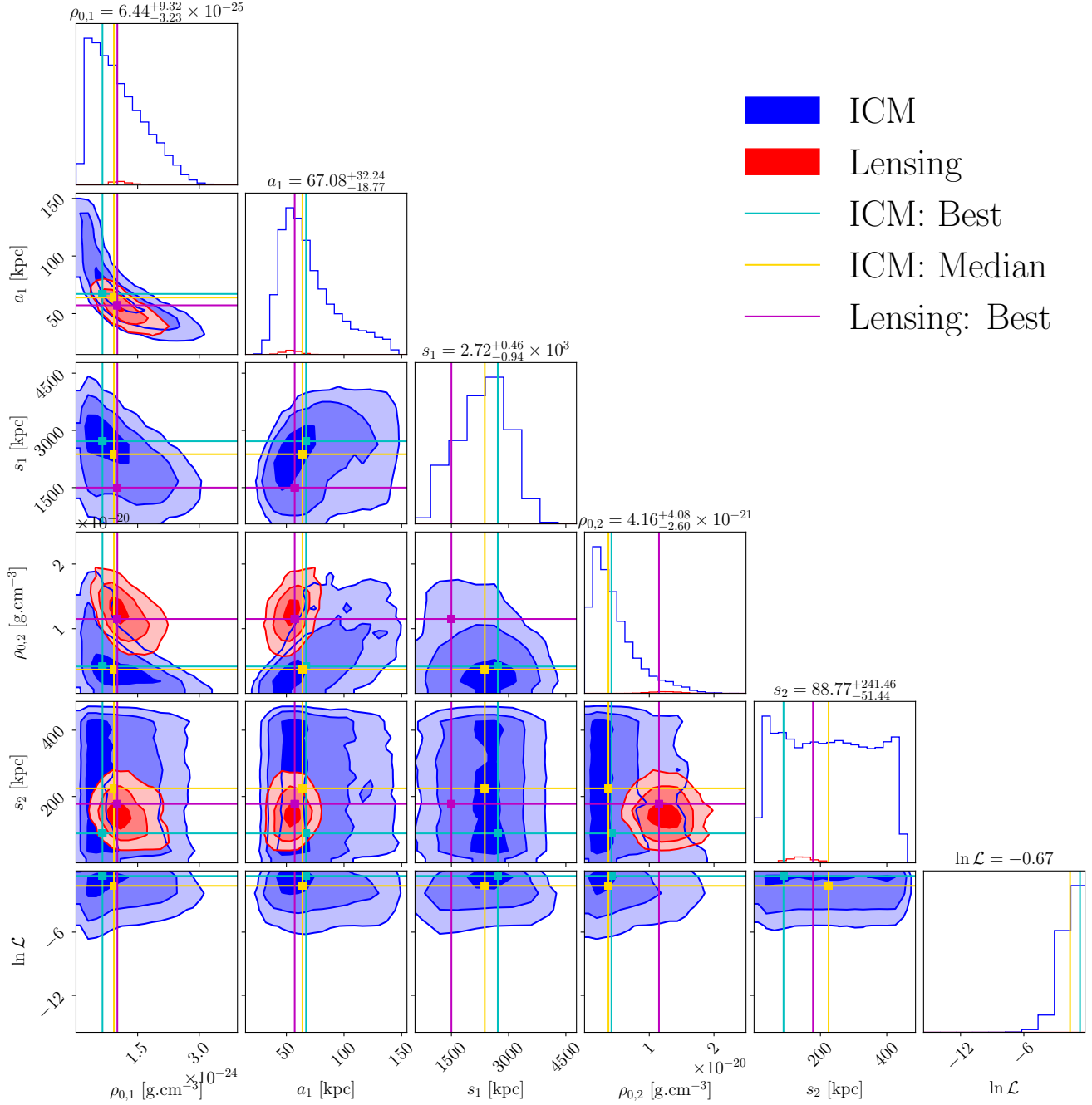


Figure E3. MCMC optimisation for idPIE model, for cluster MACSJ0242: DMH central density $\rho_{0,1}$, core radius a_1 , cut radius s_1 , and BCG central density $\rho_{0,2}$ and cut radius s_2 . Densities are displayed in g.cm^{-3} , distances in kpc. *Blue*: Optimisation performed using the available ICM data (X-ray here). *Red*: Strong lensing optimisation. *Cyan*: Best ICM optimisation. *Gold*: Median of the ICM optimisation. *Magenta*: Best strong lensing model (described in Table 2). Comparing this to Fig. 6, we can see that the s_2 optimisation is degenerated, and therefore not necessary. This explains why we fixed the s_2 value to that of lensing in Section 8.

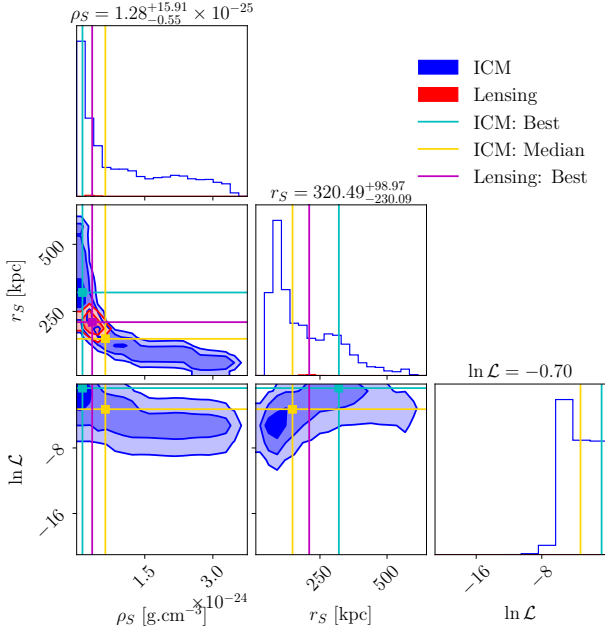


Figure E4. MCMC optimisation for inFW model of the two relevant parameters for cluster MACS J0242: the density normalisation ρ_S and the scale radius r_S . Densities are displayed in g.cm^{-3} , distances in kpc. *Blue*: Optimisation performed using the available ICM data (X-ray here). *Red*: Strong lensing optimisation. *Cyan*: Best ICM optimisation. *Gold*: Median of the ICM optimisation. *Magenta*: Best strong lensing model (described in Table 2).

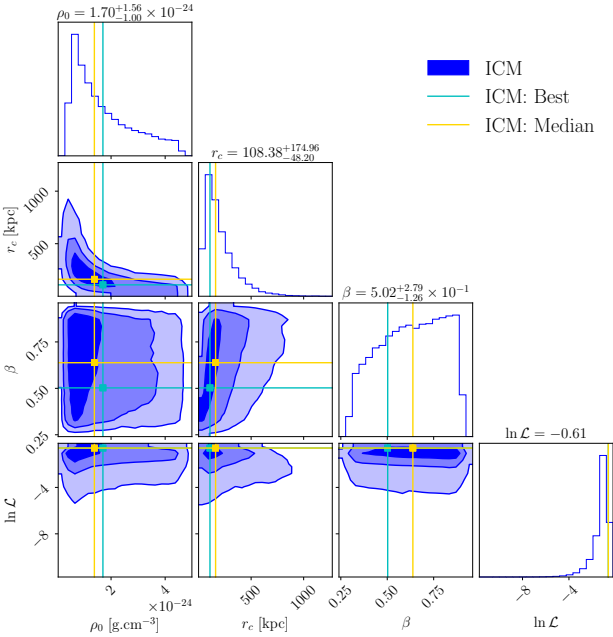


Figure E5. MCMC joint optimisation for the β model, for cluster MACS J0949. Densities are displayed in g.cm^{-3} , distances in kpc. *Blue*: Optimisation performed using the available ICM data (X-ray and SZ here). *Cyan*: Best ICM optimisation. *Gold*: Median of the ICM optimisation.

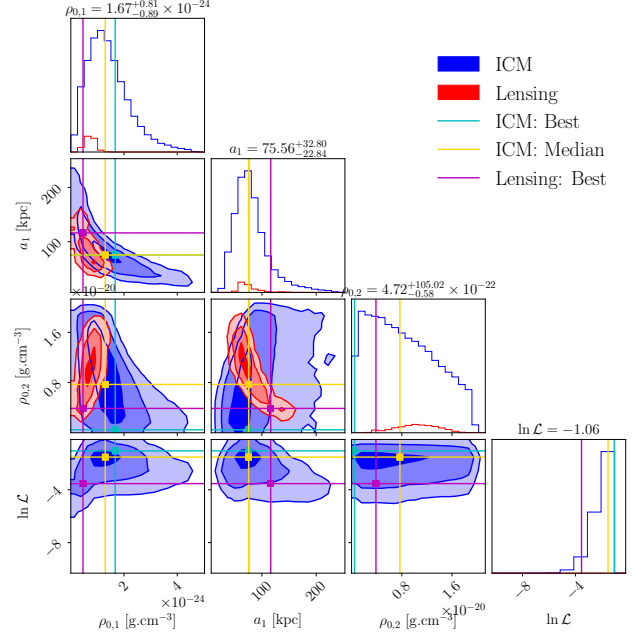


Figure E6. MCMC joint optimisation for idPIE model, for cluster MACS J0949: DMH central density $\rho_{0,1}$ and core radius a_1 , and BCG central density $\rho_{0,2}$. The DMH cut radius is fixed to the fiducial value of 1.5 Mpc. Densities are displayed in g.cm^{-3} , distances in kpc. *Blue*: Optimisation performed using the available ICM data (X-ray and SZ here). *Red*: Strong lensing optimisation. *Cyan*: Best ICM optimisation. *Gold*: Median of the ICM optimisation. *Magenta*: Best strong lensing model (described in Table 2). Similarly to Fig.E2 for MACS J0242, the comparison between this optimisation excluding s_1 and Fig. 9 displays the importance of the s_1 optimisation.

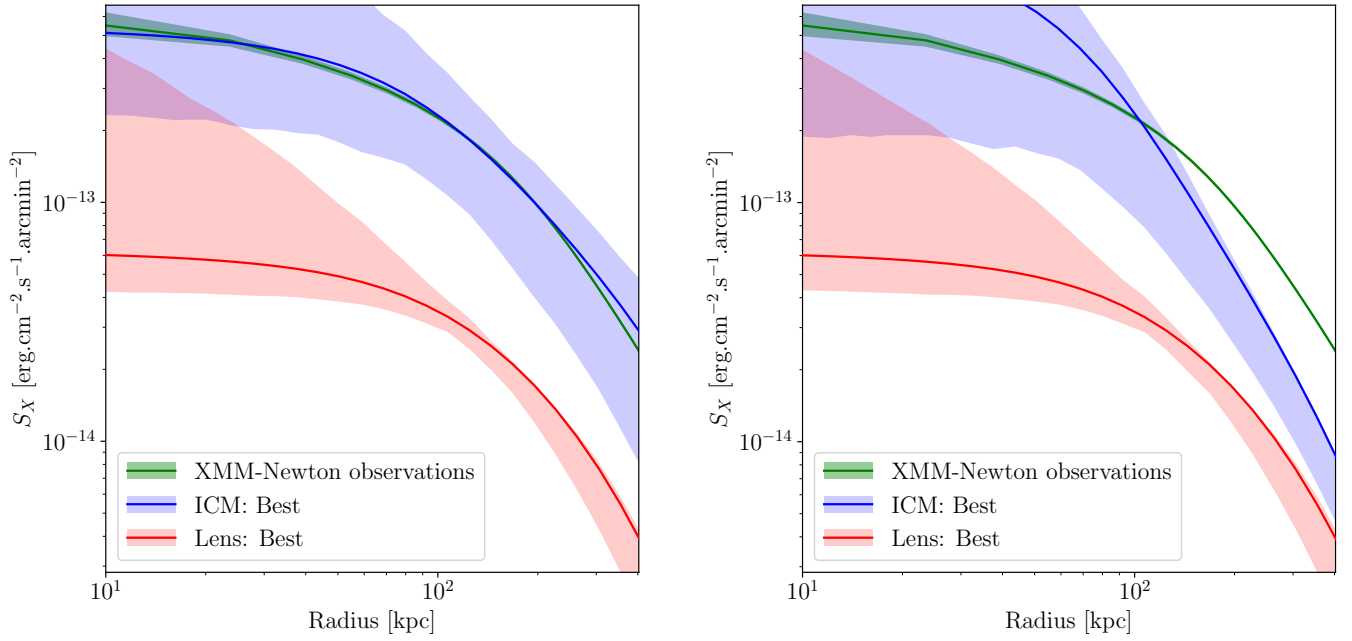


Figure E7. X-ray surface brightness S_X for idPIE model, for cluster MACSJ0949. *Green:* X-ray surface brightness deprojected profile (assuming spherical symmetry). *Blue:* Best ICM-optimised profile, with an idPIE model. *Red:* Best lens model inferred profile. *Left:* In the case of the optimisation of parameters $\rho_{0,1}$, a_1 , s_1 and $\rho_{0,2}$, as illustrated in Fig. 9. *Right:* In the case of the optimisation of parameters $\rho_{0,1}$, a_1 , and $\rho_{0,2}$, as illustrated in Fig. E6.

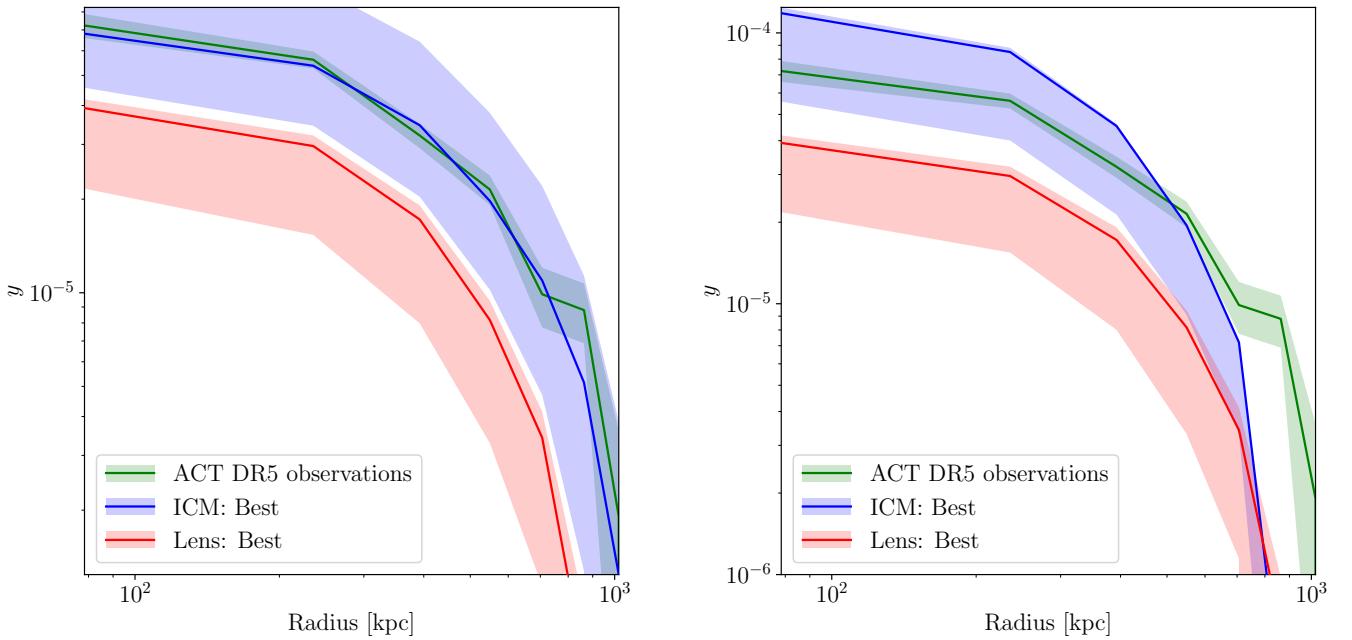


Figure E8. Compton parameter y for idPIE model, for cluster MACSJ0949. *Green:* SZ effect Compton y parameter observed profile with ACT. *Blue:* Best ICM-optimised profile, with an idPIE model. *Red:* Best lens model inferred profile. *Left:* In the case of the optimisation of parameters $\rho_{0,1}$, a_1 , s_1 and $\rho_{0,2}$, as illustrated in Fig. 9. *Right:* In the case of the optimisation of parameters $\rho_{0,1}$, a_1 , and $\rho_{0,2}$, as illustrated in Fig. E6.

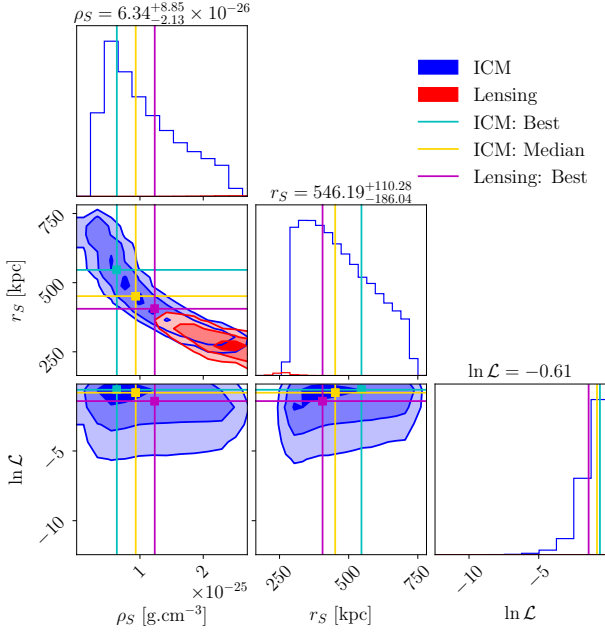


Figure E9. MCMC joint optimisation for iNFW model. The individual values for the best optimisation here presented are: $\ln \mathcal{L}_X = -0.58$ and $\ln \mathcal{L}_{SZ} = -0.90$. Densities are displayed in $\text{g}\cdot\text{cm}^{-3}$, distances in kpc. *Blue*: Optimisation performed using the available ICM data (X-ray and SZ here). *Red*: Strong lensing optimisation. *Cyan*: Best ICM optimisation. *Gold*: Median of the ICM optimisation. *Magenta*: Best strong lensing model (described in Table 2).

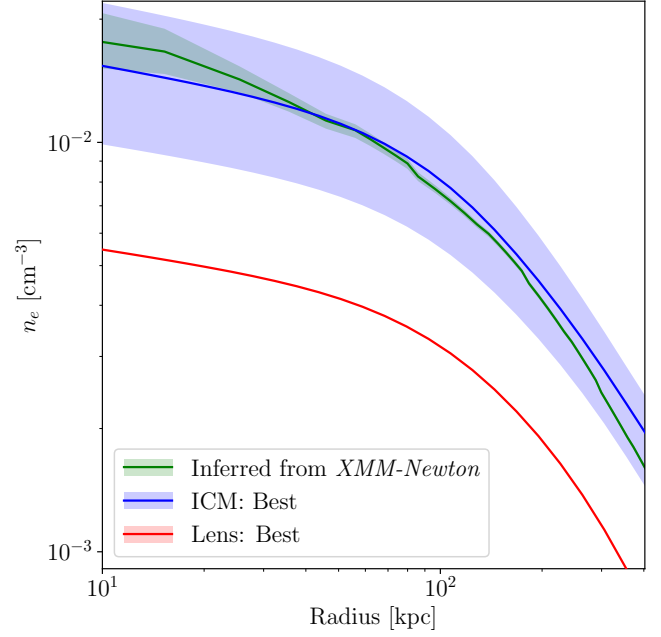


Figure E10. Electron density n_e of the ICM for the idPIE model, for cluster MACSJ0949. *Green*: X-ray surface brightness deprojected profile (assuming spherical symmetry). *Blue*: Best ICM-optimised profile, with an idPIE model. *Red*: Best lens model inferred profile. The ICM optimisation was here only performed on parameter s_1 , setting the other profile parameters to their strong lensing value. The comparison between the red and blue outlines the importance of the DMH cut radius optimisation. Indeed, the n_e density does not only change dramatically in the outskirts, but also in the centre of the cluster. This is due to the sensitivity of the function \mathcal{J}_z^{-1} and of the shape of the potential Φ , and is discussed in Sec. 8.1.